NAGW-4878

IN-46
OCIT 062

Reanalysis of Clementine Bistatic Radar Data from the Lunar South Pole

Richard A. Simpson, and G. Leonard Tyler

Center for Radar Astronomy
Stanford University
Stanford, CA 94305-9515

Submitted to *Journal of Geophysical Research*

12 March 1998

Abstract. On 9 April 1994 the Clementine spacecraft high-gain antenna was aimed toward the Moon's surface and the resulting 13-cm wavelength radio echoes were received on Earth. Using these data, we have found that the lunar surface generally follows a Lambertian bistatic scattering function $\sigma_0 = K_D \cos\theta_i \cos\theta_s$ with $K_D \sim 0.003$ for the opposite (expected) sense of circular polarization and $K_D \sim 0.001$ for the same (unexpected) sense. But there are important deviations—of up to 50% in some parts of the echo spectrum—from this simple form. Based on an earlier analysis of these same data, *Nozette et al.* [1996] claimed detection of an enhancement in echoes with right circular polarization from regions near the South Pole in a near-backscatter geometry. Such behavior would be consistent with presence of perhaps large quantities of water ice near the Pole. We have been unable to reproduce that result. Although we find weak suggestions of enhanced echoes at the time of South Pole backscatter, similar features are present at earlier and later times, adjacent frequencies, and in left circular polarization. If enhanced backscatter is present, it is not unique to the South Pole; if not unique to the Pole, then ice is less likely as an explanation for the enhancement.

1. Introduction

During April 1994 a set of bistatic radar (BSR) observations was carried out using the Clementine spacecraft. Continuous wave S-band (13 cm wavelength) signals in right-circular polarization (RCP) were transmitted from the spacecraft. The spacecraft high-gain antenna (HGA) was aimed at the lunar surface; radio echoes were captured with 70-m antennas at stations of the NASA Deep Space Network (DSN). Signals in both RCP and left-circular polarization (LCP) were received, converted to baseband, sampled coherently, and recorded using an open-loop receiving system at the DSN station.

A primary objective of the experiments was detection and measurement of radio echoes in a near-backscatter geometry from possible deposits of water ice in permanently shadowed areas on the lunar surface [*Nozette et al.*, 1996]. Such deposits would, it is believed [*Hapke and Blewett*, 1991], have distinct angular and polarization ratio scattering signatures, similar to those detected previously in the polar regions of Mercury and Mars and from the surfaces of Callisto, Ganymede, Europa, and (possibly) Titan [*Muhleman et al.*, 1995]. Observing times for the Clementine experiments were chosen so that one of the Moon's polar regions would be visible from Earth and, simultaneously, the Earth would be close to the spacecraft's orbit plane. During experiments on 9-10 April the Clementine HGA was aimed toward the South Pole (Figure 1); on 23-24 April the HGA was aimed toward the North Pole. *Nozette et al.* [1996] reported a 1 dB enhancement in RCP South Pole echoes for small bistatic angles ($\beta_{sp}<1°$) on orbit 234. Their announcement prompted widespread discussion, including challenges based on Arecibo monostatic radar data [*Stacy et al.*, 1997] and polar topography models [*Smith and Zuber*, 1997].

After independent analysis of the Clementine data, we are unable to reproduce the results published by Nozette *et al.* Here we review the experiment design and execution, paying particular attention to observing geometry and data calibration. We also describe our analysis and summarize the results. Although our conclusion is negative, it is not in conflict with the presence of ice—only the existence of ice in nearly pure form and in large quantities as inferred from this particular experiment.

2. Experiment Design

Received power following bistatic scattering from a target surface may be computed using the radar equation

$$P_R(f) = \int_{A(f)} \frac{P_T G_T(\theta_T)}{4\pi|t|^2}\, \sigma_0(\theta_i,\theta_s,\beta)\, \frac{\lambda^2 G_R(\theta_R)}{(4\pi)^2|r|^2}\, dA(f) \tag{1}$$

where f is frequency and the other quantities are defined in Table 1 [*Simpson,* 1993]. Integration is performed along loci of constant frequency over the surface mutually visible from both transmitter and receiver; in this way Doppler frequency variations over the surface are mapped into the echo spectrum. The specific radar cross section σ_0 quantifies scattering from a surface element of unit area under a range of geometrical conditions; for convenience, we have suppressed possible spatial variations of σ_0 in (1).

Although the intrinsic sensitivity of the Clementine experiment was more than five orders of magnitude below what could be achieved with Earth-based radar (Table 1), the experiment's geometry uniquely allowed continuous monitoring of the scattered signal as a function of bistatic angle

$$\beta_{sp} = \arccos\left(\frac{-\mathbf{t}_{sp}\cdot\mathbf{r}_{sp}}{|\mathbf{t}_{sp}||\mathbf{r}_{sp}|}\right) \tag{2}$$

where β_{sp} is the included angle between vectors $\mathbf{t_{sp}}$ and $\mathbf{r_{sp}}$ from the South Pole to transmitter and receiver, respectively (Figure 1). More generally, β is the included angle between vectors $\mathbf{t}$ and $\mathbf{r}$ from any point on the surface to the transmitter and receiver. Although there existed a locus of points $\beta=0°$ on the surface any time Clementine passed in front of the lunar disk as seen from the receiving location, polar regions were accessible at small β only when the receiver and the polar target area were both nearly in the spacecraft orbit plane. At those times, it was possible to search for subtle changes in the near-backscatter radar response—a dependency that cannot be observed with a purely monostatic system, for which β is identically zero everywhere.

Data were collected on Clementine orbit 234 (9 April 1994) using the 70-m DSN antenna near Barstow, California. The track of $\beta=0°$ points passed within 5 km of the South Pole on this orbit (Figure 2); the minimum bistatic angle for the Pole itself was $\beta_{spmin}=0.1°$ at $t_0 = 18:46:36.5$ (Figure 3). The HGA began pointing toward the South Pole approximately 30 minutes before t_0, while the spacecraft was still well below the polar horizon. Observations continued for more than an hour after t_0, by which time the South Pole bistatic angle had grown to β_{sp}~90°. Figure 3 shows South Pole incidence, scattering, and bistatic angles as a function of time during a 16-minute period centered approximately on t_0. Except for discussing overall system amplitude calibration, we will henceforth limit our attention to this 'primary' interval, which corresponds to a single data tape.

Figures 4 and 5 show important parameters as functions of surface location at three distinct times during the 16-minute interval. For these calculations we represented the Moon as a uniform sphere of radius 1737.4 km; effects of topography, which are important but poorly known in the polar areas, were ignored. Figure 4 shows angular variations, antenna illuminations, Doppler frequency, and signal strength contours at t_0; Figure 5 shows bistatic angle, Doppler frequency, and signal strength contours 500 seconds earlier and 300 seconds later than t_0. Dashed lines show circles of constant latitude γ; the unlabeled "+" in each panel indicates the South Pole, the closed circle is at 85°S, and succeeding circles are in 5° latitude steps toward the equator.

Figures 4a and 4b show contours of incidence and scattering angle, respectively. The contour interval is 5°; no contours are shown beyond 90°, the respective horizon as seen from the transmitter or receiver. Figure 4c shows distribution of bistatic angle; here the contour interval is 1°, with the innermost contour encircling surface elements for which $\beta \leq 1°$—a majority of the surface poleward of 85°S, but also including elements from as far as 78°S. Figures 4d and 4e show projected antenna beams for transmitter and receiver, assuming both antennas were aimed at the South Pole. The transmitter beam covers a larger solid angle than the receiving beam (Table 1); but, because the spacecraft is much closer to the target, G_T controls the effective area contributing to the bistatic echo in this case. Note that contour levels for the transmitter beam are larger (5 dB) than for the receiver beam (2 dB).

The elliptical contours in Figure 4f show results of evaluating the radar equation (1) at each grid point. Only those parts of the surface mutually visible to both transmitter and receiver (θ_i, $\theta_s \leq 90°$) can contribute to a bistatic surface echo. The line "Mutual Terminator" shows the conjoint limit of visibility. The radar cross section at a grid point was taken to be $\sigma = \sigma_0 dA$ where $dA = 25 \cdot 10^6 \csc\gamma \, m^2$ and we have set $\sigma_0 = 1$ to obtain evaluation of the radar equation for all quantities except the scattering function. By carrying out the calculation for a number of other possible scattering functions $\sigma_0(\theta_i, \theta_s, \beta, \ldots)$, we also built a suite of P_R templates for comparison with data; but we will defer the question of alternative σ_0 forms to later.

Figure 4f also shows approximately circular contours of Doppler shift. Each point on the surface can be associated with a Doppler shift which results from relative motions among the spacecraft, receiver, and surface. The frequency shift relative to the South Pole target is

$$f_D = \frac{|\dot{\mathbf{t}}_{sp}|+|\dot{\mathbf{r}}_{sp}|}{\lambda} - \frac{|\dot{\mathbf{t}}|+|\dot{\mathbf{r}}|}{\lambda} \tag{3}$$

where dots denote time rate of change of vector magnitudes. Summing received power for each grid point dP_R after sorting by the associated Doppler shift f_D allows construction of a model echo power spectrum $P_R(f)$, as was noted above. In Figure 4f, the Doppler contours are spaced by 12.2 Hz, eight times the width of Doppler bins in our final analysis (see below). The South Pole and about half of the area poleward of 85°S are responsible for echo power in the next-to-highest frequency bin ($|f_D| \leq 6.1$ Hz). The Doppler separation between the South Pole and the Mutual Terminator is about 8 Hz. A very small area at the back (anti-Earth) side of the 85°S cap goes into the highest bin ($6.1 < f_D < 18.3$ Hz), while the forward section of the cap plus an approximately equal area from the 80-85°S annulus fill the bin immediately below the South Pole in frequency ($-18.3 < f_D < -6.1$ Hz). The mapping of Doppler bins onto the surface becomes more difficult to describe at lower frequencies, but the next four lower bins are predominantly from the 80-85°S ring.

At t_0–500 the shape of the dP_R contours (Figure 5b) is similar to the shape at t_0 (Figure 4f). Note, however, that the Mutual Terminator is Earthward of the South Pole, reflecting the fact that the spacecraft had not progressed as far in its orbit as in Figure 4. The highest frequency Doppler bin with non-zero echo power very nearly overlays the 85°S cap; that bin ($|f_D| \leq 6.1$ Hz) would contain echo contributions from the South Pole itself except that the Pole is not illuminated by the spacecraft beam ($\theta_s > 90°$). The $\beta = 0°$ point, meanwhile, lies on the 55°S latitude circle (Figure 5a); over the next 500 seconds, it moved slowly poleward and β contours became elongated until they matched Figure 4c.

At t_0+300 the dP_R contours (Figure 5d) are also very similar to their shapes at t_0 (Figure 4f). The mutual terminator is at the same point behind the South Pole, but it has been pushed back to the Earth horizon on the left and right as the spacecraft moves closer to the Pole. The Doppler separation between the South Pole and Mutual Terminator is now approximately 16 Hz, and the smallest bistatic angles are $\beta\sim3°$ on the far side of the Pole as viewed from Earth (Figure 5c).

From Figure 2 it is apparent that the $\beta=0°$ point moves quickly once it is in the vicinity of the South Pole. On the other hand, from Figure 3 it is also clear that the South Pole itself is illuminated at bistatic angles less than 1° for approximately 200 seconds, centered on t_0 = 67596.5. In addition to the South Pole, however, the $\beta\leq1°$ region is large—nearly two-thirds of the area between 85°S latitude and the Pole, plus additional area extending on the Earth side of the Pole to at least 78°S (Figure 4c). The $\beta\leq1°$ region can be resolved in Doppler; but the 'footprints' are approximately circular annuli typically 500 km long with widths proportional to the Doppler resolution. With 12.2 Hz resolution, the footprints are 'horseshoes' approximately 500 km long by 60 km wide; at 1.53 Hz resolution the footprints are 500 km by 8 km.

3. Execution and Calibrations

The objective in collecting and analyzing the Clementine bistatic data was to measure the variation of $P_R(f_D\sim0)$ near t_0. Since both the amplitude and frequency calibration steps are important to the final result, we devote this section to a more detailed discussion of each.

The receiving and recording system for each polarization is shown in simplified form in Figure 6a; RCP and LCP chains operated in parallel. Input to the maser could be switched between the 70-m antenna and a calibration ambient load. The programmable oscillator was tuned to ensure that the signal of interest remained within the output passband. During the 16-minute 'primary' interval, tuning predictions were updated each minute. Real 8-bit samples were merged from both RCP and LCP and written to digital tape for later processing. The 8-bit samples represented a bandwidth of 25 kHz for each polarization.

The steps in processing are summarized in Figure 6b. Tape data were sorted so that RCP and LCP samples were again in separate, but still coherent, streams. Compensating filters created flat output spectra in response to white noise inputs on both channels. Gain adjustments were applied to correct for known attenuator changes during data acquisition and to calibrate the noise levels in each channel against a standard noise source. In two steps we adjusted sample phase so that echoes from the frequency bin corresponding to the South Pole had a constant frequency. We then extracted the echo power in that bin for interpretation. The bandpass filter in Figure 6b represents our monitoring of processing and data quality at any stage (not just the explicit point shown in the figure).

Figure 7 shows power in raw data samples. A pure sinusoid with amplitude equal to the input limits of the analog-to-digital converter (ADC) would appear as a straight line at 0 dB in each panel. Events B, F, and G occurred within 40 seconds of t_0 (β_{sp}~0.4°). Figure 8 shows RCP power spectra over the 16-minute "primary" interval; each curve is an average over 60 seconds. For the data described here, our monitoring and calibration (previous paragraph) was based on noise in the frequency range 17000-20125 Hz, which was above both carrier and surface echo frequencies on orbit 234. Note that Figures 7 and 8 are both plotted on logarithmic vertical scales.

3.1. Equalizing Filters

We designed a pair of simple digital filters based on samples collected during a noise-only calibration. These filters were defined in the frequency domain; the amplitudes were set to the inverse square root of the noise power spectral density over a 304 second interval, and phases were made linear with frequency corresponding to a constant delay over the filter passband. These steps removed a 15% ripple in the baseband output and ensured that gain would be constant (better than 1%) over the central 80% of each passband. The equalization was applied while we converted the original samples to complex floating point values. With floating point numbers we were no longer limited in dynamic range; through several steps, discussed in more detail below, we calibrated the sample value magnitudes for each polarization against a standard reference.

3.2. Relative Gain Calibrations

During Clementine operations, attenuators were used to ensure that ADC inputs remained well below their saturation levels. The reductions indicated by A and B in Figure 7 correspond to 1 dB increases in the RCP attenuator settings, keeping the raw sample power comfortably below 0 dB. Close examination of the data shows the signal at A and B disappearing entirely for about 5 msec at the time of each adjustment, then returning at the reduced level. These level changes can be confirmed by checking header information in the data records; the attenuator settings were polled asynchronously (typically every few seconds) and current values were saved along with the data samples. Following conversion of 8-bit samples to floating point and application of the equalizing filters, we increased the sample amplitudes after A by 1 dB and after B by 0.8 dB. The level at B was not adjusted by a full dB because later investigation showed that the hardware implementation of this particular step resulted in only a 0.8 dB change in noise level (see below).

The first four level changes in LCP (Figure 7, events C through F) show the 5 msec drop-out and 1 dB net reduction expected of attenuator changes. Event G, by contrast, is a reduction of about 0.7 dB that occurs continuously and smoothly over an interval of about 0.8 seconds. Curiously, the four attenuator changes recorded in the data headers match events D through G to within three seconds, whereas forcing agreement with C through F means that the polling results would have been delayed by much more—204 seconds in the worst case. We have no good explanation for this discrepancy. By examining data after bandpass filtering (Figure 6b) we have confirmed that power levels in noise-only portions of the spectrum match behavior of the raw samples at all five event times; so there is no question that system gain changed in each case. Despite not having good confirmation from the data record headers, we have proceeded on the assumption that C through F are valid attenuator changes and have increased the floating point sample amplitudes by 1 dB after each.

Event G in Figure 7b may be a spontaneous gain change in either the LCP maser or a later amplifier. The LCP receiving system is used infrequently, and intermittent problems at this level might go unnoticed for some time. During the 40 minutes following G we saw other changes of comparable magnitude in LCP, though over time scales of tens of seconds to a few minutes, rather than the 0.8 sec at G. There was never a corresponding change in the RCP level. Since all parts of the LCP spectrum were affected equally, we have modeled G and the later changes as though they were piecewise linear changes in gain. The results are satisfactory from a signal self-consistency point of view, but leave some uncertainty as to the absolute amplitude calibration of the LCP channel. Since it is anomalous behavior in RCP that is most strongly related to the interpretation of the presence of ice, the practical impact of these LCP fluctuations on the ice question is minimal.

3.3. Absolute Gain Calibrations

Both before and after the surface observations on orbit 234, the system noise temperature (T_{sys}) for each receiver was obtained by comparing emissions from 'dark' sky (T_{sky}) against power generated by an ambient load (Figure 6a). Both sets of calibration measurements were made near midday local time with the antenna pointed to zenith. Although the physical temperature of the ambient load was not recorded, the air temperature was reported as 58F at 19:47 UTC (71220 s); lacking a better estimate, we take 58F to be the ambient load temperature (T_{amb}) for both calibrations.

In addition, prior to the post-experiment ambient load measurement, the ground antenna was pointed toward the center of the Moon for several minutes to estimate its equivalent blackbody temperature (T_{ctr}). Since the Moon should appear equally 'bright' in both RCP and LCP, this measurement served as confirmation of the ambient load results. Because the Moon occupied roughly half of the 70-m antenna beam during South Pole measurements, the center-of-Moon measurements also provided a reference for estimating the effective contribution of the lunar limb (T_{lim}) while bistatic radar echoes were being received. The angular separation between Sun and Moon during these measurements was about 14°; we have ignored contributions from the Sun.

The full set of calibration measurements is summarized in Table 2. Measurement intervals are denoted by Rnn ($1 \leq nn \leq 20$) for RCP and Lnn ($1 \leq nn \leq 22$) for LCP. Intervals are not contiguous because of breaks between data tapes, allowance for settling after attenuator changes, and because of the instability in LCP gain noted above. The Mean Measured Noise Power was adjusted by the effective attenuator setting to give the Adjusted Mean level in the next-to-last column of Table 2. Measurements of the same 'target' were weighted and averaged to give values in the final column.

RCP values in Table 2 were measured with respect to a common amplitude reference; LCP values were also made with respect to a common, but different, reference. The two polarizations were compared against each other later (see below). Attenuation in each polarization was increased by about 10 dB during ambient load measurements so that approximately the same voltage levels would be seen by the ADC. Although attenuators operated only in integer steps, our analysis showed that not all steps were equal. The transition from 39 dB to 40 dB was implemented by removing several small attenuation steps and substituting a single 40 dB attenuator. By comparing noise power before and after such transitions, we concluded that the nominal 40 dB attenuation actually differed from the nominal 39 dB level by only 0.8 dB. The 39.8 and 40.8 dB entries in column 6 of Table 2 are our corrections to the 40 and 41 dB nominal values. There were no comparable adjustments for LCP; but we have modeled three of the 'unstable' intervals as having effective attenuator settings of 42.7 dB.

Following standard practice, we employed three 'Y factors' where numerators and denominators correspond to measured quantities. Y_1 is the ratio of power when the maser was connected to the ambient load to power when the maser was looking through the antenna at 'dark' sky (Figure 6a). Y_2 and Y_3 are the corresponding quantities when center-of-Moon and lunar limb measurements, respectively, appear in the denominator. We do not identify separately contributions to measured values from the antenna and its feed, Earth's atmosphere, or 'dark' sky when observing the lunar limb.

$$Y_1 = \frac{T_{sys} + T_{amb}}{T_{sys} + T_{sky}} \tag{4}$$

$$Y_2 = \frac{T_{sys} + T_{amb}}{T_{sys} + T_{ctr}} \tag{5}$$

$$Y_3 = \frac{T_{sys} + T_{amb}}{T_{sys} + T_{lim}} \tag{6}$$

If T_{sky} is known, equations (4)-(6) can be solved for T_{sys}, T_{ctr}, and T_{lim} using values in the last column of Table 2.

The result of interest for a receiving system observing a distant point source is the sum $T_{sys} + T_{sky}$, the background noise level if the antenna is pointed at dark sky. Solving equation (4) for several assumed values of T_{sky} yields the effective system temperatures shown in Table 3, where we show T_{sys} based on both pre-experiment and post-experiment calibrations. The nominal 'big bang' background ($T_{sky} = 2.7K$) should be increased slightly to account for antenna and feed effects, but the sum $T_{sys} + T_{sky}$ is only weakly sensitive to T_{sky}. We have adopted 21.51K and 20.12K as working values of system temperature for RCP and LCP, respectively. Although reproducibility between pre-experiment and post-experiment ambient load calibrations is better than 1% we feel that systematic errors (lack of knowledge of the physical ambient load temperature, 2% quoted accuracy in attenuator values, etc.) makes these working values accurate at the ±1K level.

Based on our adopted system temperatures, we would expect the dark sky observations to be 0.29 dB 'hotter' on RCP than LCP. In fact, the pre-experiment and post-experiment sky measurements from RCP were 3.05 dB higher (Table 2). Increasing all LCP sample values by 2.76 dB would bring both polarizations to the same absolute amplitude reference; that blanket correction was applied in the 'GAIN' stage of our processing (Figure 6b).

Measurements obtained when the 70-m antenna was pointed to the center of the Moon ($T_{sys} + T_{ctr}$), as well as measurements of microwave radiothermal noise when the lunar limb filled half of the 70-m antenna beam ($T_{sys} + T_{lim}$), are also listed in Table 2; derived values (parameterized by T_{sky}) are shown in Table 3, where we have used the post-experiment ambient load measurements as the reference. We would expect T_{ctr} for the two polarizations to be equal, since emission from the Moon is unpolarized; the ~2.5K difference (±1%) suggests that our calibration has been effective but is not perfect.

From comparison of T_{ctr} and T_{lim} it is apparent that the Moon is limb dark. Slightly more than half of the beam should be filled by the Moon during South Pole observations, yet T_{lim} is only about one-third of T_{ctr}. More interesting is the fact that T_{lim} for RCP is less than the corresponding value for LCP. Mike Wert of the DSN (private communication, 1998) has predicted that there should about a 0.02 degree angular offset between the boresights of the two circular polarizations at S-Band from 'squinting' in the feed systems. Since the half-power full beamwidth of the 70-m antenna at S-Band is 0.108 degrees, the difference in power under our observing conditions could be as little as 0% or as large as 18.5%, depending on the direction of the squint offset relative to the limb. Our observed difference is at the high end of this range and would be consistent with an elevation-only squint offset.

3.4. Frequency Calibration

Historically we have relied on high-stability crystal oscillators aboard spacecraft to provide a frequency reference for bistatic radar experiments; residuals during Voyager experiments were typically at the milliHertz level [*Tyler*, 1987]. Clementine was not equipped with a precision oscillator, however; so we used a smoothed version of the received carrier frequency itself as a reference and then located the frequency bin containing echoes from the South Pole relative to the carrier.

The Doppler shift of the signal propagating directly from transmitter to receiver is

$$f_c = -\frac{\mathbf{r}_{sp}-\mathbf{t}_{sp}}{|\mathbf{r}_{sp}-\mathbf{t}_{sp}|} \cdot \frac{\dot{\mathbf{r}}_{sp}-\dot{\mathbf{t}}_{sp}}{\lambda} \tag{7}$$

where quantities are as defined earlier. The signal reaching Earth by way of the South Pole has a Doppler shift

$$f_{sp} = -\frac{|\dot{\mathbf{t}}_{sp}|+|\dot{\mathbf{r}}_{sp}|}{\lambda} \tag{8}$$

Doppler shifts for other points on the surface, relative to the South Pole shift, are given by (3).

We estimated the carrier frequency from the RCP data using 4096 complex samples in zero-padded 16384-point voltage spectra (1.53 Hz resolution), averaged those over 1 sec time intervals. We then used the measured frequencies to derive a piecewise linear continuous frequency function and adjusted the sample phases so that the carrier would appear at 12500 Hz. In fact, the oscillator was not well-behaved; but differences between successive frequency estimates were rarely larger than 2 Hz. After phase adjustment, the measured RCP carrier frequency was 12500.0015±0.9253 Hz (Figure 9).

We compared independent RCP and LCP frequency estimates and found that they agreed to within 0.1 Hz. Although from the same source, these two signals could be viewed as having been radiated separately in the anti-boresight direction; in the receiving system they passed through different amplifier chains and were subject to independent noise processes. The close agreement between the frequency estimates in the two polarizations suggests that the 0.9253 Hz standard deviation after phase adjustment is a measure of the carrier instability on time scales of 0.1-1.0 sec rather than a limitation in our frequency estimation software.

We also fitted a second-degree polynomial to carrier frequency estimates over our 16-minute primary interval. Residuals with respect to the quadratic were about 3 Hz rms, with the same drift patterns visible in plots from both polarizations.

From this work we concluded that the estimation, averaging, and phase adjustment procedure outlined above was adequate to locate the Clementine carrier frequency to approximately ±1 Hz in the spectrum. The accuracy with which a South Pole frequency bin can be identified is comparable, limiting useful transform lengths to 16384 and less.

From ephemerides of the spacecraft, Moon, and receiving station we computed the expected Doppler shift on the direct signal and on scattered signals from the South Pole; the difference $\delta f = f_{sp} - f_c$ then gave the expected offset frequency between the carrier and the South Pole echo. We used δf to adjust the phases of the complex time samples one more time so that the South Pole bin would be fixed at the center of the passband (12500 Hz). We then searched power spectra derived from these samples for evidence of enhanced echoes from the South Pole.

4. Analysis

4.1. Search for Enhanced Backscatter from the South Pole

After amplitude and frequency calibration of the data, we created power spectra from samples in both polarizations. The original processing by *Nozette et al.* included four-second incoherent averaging of 16384-point power spectra and smoothing in time with a median filter of order 60 (Lichtenberg, private communication, 1998). For our own analysis we chose 16384-point power spectra with no averaging; we discuss filtering below. We extracted 1024 bins from each spectrum for detailed study; these included the South Pole bin (now fixed at 12500 Hz as a result of our frequency calibration), 966 bins at lower frequencies which contained the majority of the surface echo, and 57 bins at higher frequencies to establish a radiothermal noise reference (most of these bins contained no surface echo). For our 'primary' interval this yielded an array with dimensions 1024 in frequency by 1464 in time. We combined the $T_{sys}+T_{lim}$ amplitude calibration results (Table 3) with measured levels at 56560 points in the noise-only portion of the array to scale the spectra to power density (watt/Hz) in each polarization and examined the results.

Figures 10a and 10b show echo strength in 22 contiguous frequency bins as a function of time for RCP and LCP, respectively. The bold line denotes our best estimate of the frequency bin containing the South Pole; lower frequency bins (Earthward of the Pole) are plotted above, while higher frequency bins are plotted below. Annotations on the extreme curves indicate their frequency offsets from the South Pole. To reduce statistical fluctuations in the echo power, we have applied a 100 sec running average (153 points) to each curve. Shorter averages leave more structure on each curve, but the result is qualitatively similar. Longer averages lead to more smoothing, but with increasing potential for loss of the enhanced backscatter anomaly since the $\beta \leq 1°$ opportunity is only about 200 seconds (Figure 3). The lower left corner of each figure contains only noise; those frequencies are too high to correspond to echoes from the lunar surface (Figure 5b). From Figure 5b we noted that the South Pole itself was slightly beyond the highest Doppler contour observable on a smooth, spherical Moon at t_0-500 sec; the fact that three or four higher bins appear to have small amounts of echo power could be the result of (positive) topography in the vicinity of the South Pole. The appearance of echo power at frequencies higher than the South Pole toward the end of the interval (lower right corner of each figure) is consistent with slow migration of higher frequency contours onto the surface (Figure 5d).

We have examined these curves, and others like them, at a number of resolutions in both time and frequency. We have used median filters as well as simple running means, with no qualitatively different results. In each case, there is a considerable amount of structure present in the curves; but we have found nothing that is uniquely or even strongly diagnostic of enhanced backscatter from the South Pole region. Among the better candidates is a peak in the curve at the lowest frequency in Figure 10a. The peak is close to the South Pole backscatter condition (t_0+25 sec), and the peak-to-trough difference in amplitude is about 1.7 dB, nearly twice the enhancement shown in Figure 3 of *Nozette et al.* [1996]. But the -18.31 Hz frequency offset from the South Pole puts the corresponding surface on the second contour outside the closed circle in Figure 4f and no closer to the Pole than about 86°S. This places it outside the search area identified by *Nozette et al.* [1996] in their Figure 4. Further, the peak at t_0+25 sec is only one of four visible in that frequency bin, three of which have clear companions in LCP (Figure 10b).

Another possible enhancement near t_0 in Figure 10a is in the eighth curve above the bold line (offset -12.21 Hz) with a broad peak centered near t_0-40 sec. In this case the peak-to-trough difference is also about 1.7 dB and, again, there is a companion increase of about 1.4 dB in LCP.

The South Pole bin itself shows a local maximum starting at about t_0–60 sec, but extending for more than 200 seconds. There are also peaks in the bins at higher frequency than the South Pole; but the peaks occur well after the $\beta=0°$ point has left the lunar surface (Figure 2). None of these features stands out with the clarity or uniqueness of the RCP/LCP pair identified from orbit 234 in Figure 3 of *Nozette et al.* [1996].

4.2. Scattering Function

In computing dP_R contours shown in Figures 4 and 5 we set specific radar cross section to unity ($\sigma_0 = 1$). Table 4 lists three other functions for which we have numerically evaluated the radar equation (1) over our grid at t_0. The numerically calculated spectra are shown in Figure 11, scaled for presentation on a common set of axes. Although the constant function (curve 'A' in Figure 11) was useful for identifying regions on the surface with potential for contributing to echoes, it is not a realistic candidate for the actual scattering function. The two cosinusoidal functions ('B' and 'C') yield similar spectra, largely because the distributions of θ_i and θ_s over the surface are very much the same near t_0. The Lambertian function has the smallest response near the limb but becomes relatively stronger at Doppler shifts of more than 200 Hz from the South Pole.

We obtained average spectra for both RCP and LCP over the 100 sec bracketing t_0. Those data curves, plus the best Lambertian fits, are shown in Figure 12. Structure in the spectra such as the peaks in both polarizations at −30, −100, −210, and −460 Hz is as much as 50% of the total return at some frequencies and makes none of the fits particularly good. The RCP fit residual, expressed as rms error, is in the range 3.5e-21 watts/Hz for all three models. The LCP residual is about twice as large for the Lambertian and about three times as large for the two cosine models. The best fit coefficients for each model are shown in Table 4. The ratio of coefficients is about

3.1-3.2 (in favor of LCP), a result that is consistent with the ratio of data spectra (not shown) but somewhat larger than ratios based on much earlier monostatic work [*Hagfors and Evans*, 1968].

5. Discussion

Although we have tried to parallel the processing carried out by Nozette and colleagues, our methods have not been identical—in part from lack of detailed knowledge of their procedures, but also because we felt improvements could be made at certain stages. We review three differences in our processing, then we discuss the implications of our results.

First, our methods for locating the South Pole echoes in power spectra differed. Nozette *et al.* located the carrier signal in power spectra, averaged over as much as four seconds; with the carrier as a reference, they found the position of the bin corresponding to the South Pole and searched for anomalous echoes in the vicinity. Based on our analysis, uncertainty in the location of the South Pole frequency bin is dominated by instability of the spacecraft oscillator and will be on the order of a few Hz on time scales of seconds. For comparison, the bin width in 16384-point power spectra is 1.53 Hz. Quantization error in choosing between discrete frequency bins would have increased slightly the overall uncertainty faced by *Nozette et al.* In our analysis we found the average carrier frequency on one-second centers, using that estimate to adjust the phases of data samples and center the carrier. We used a second stage of tuning based on calculated differential Doppler between carrier and South Pole to center the latter. By our own measurements, we believe we have located the spherical South Pole to ±1 Hz rms with most of the uncertainty arising from oscillator instability. Although our uncertainty may be somewhat better than that of Nozette and colleagues, we do not believe the difference accounts for our inability to detect the RCP enhancement. In fact, our lower uncertainty should have made detection somewhat easier.

Second, our procedures for amplitude calibration of the data differed. *Nozette et al.* used running estimates of system temperature and gain from individual power spectra. In a dynamic (but linear) system, this approach offers advantages since the amplitude calibration may be carried out automatically as the spectra are generated. They used the pre- and post-experiment ambient load measurements for absolute calibration. Our calibration was more extensive, including equalization filters to flatten spectral response, correction for attenuator changes, and end-to-end amplitude adjustments referenced to an absolute standard on both polarizations. We believe our estimates of system temperature are accurate at the ±1K (±5%) level based on self-consistency checks. The major claim of the *Nozette et al.* report, however was a *relative* change in the RCP echo level. So long as the integrity of the calibration is maintained over the time period of interest, there should be no difficulty in sensing relative changes in signal level regardless of the calibration method. Thus, we might have been in a better position to quantify an anomalous echo once detected; but either approach should have led to detection if the signal were present.

Third, our filtering of high resolution data differed. Nozette *et al.* used a median filter for detection. Median filters are non-linear; they are frequently applied to data streams with unpredictable (and often large) outliers. Radar scattering can sometimes be visualized as an interference process in which signals with various amplitudes and phases are summed; although the signal voltages may have gaussian distributions, the powers that result may not—except in the limit of large numbers. A median filter could be used to screen out the most extreme power values, perhaps allowing detection of a subtle but enduring change in target properties that would be masked by the 'noise' represented by outliers. We used both 'boxcar' and median filters in our analysis and found little qualitative difference in the results; peaks found by one filter were also found by the other when the filter lengths were equivalent. Since we prefer linear smoothing procedures, we have emphasized our boxcar results here; but neither filter revealed the desired enhancement in our analysis.

Ours is not the first challenge to the ice detection claim from *Nozette et al.* [1996]. *Stacy et al.* [1997] compared high-resolution Arecibo radar images from the South Pole and elsewhere. They concluded that most anomalous backscatter could be explained from image context—as debris at the base of crater walls, for example. None of the areas they classified as anomalous (high backscatter and high circular polarization ratio) were larger than 1 km^2. Although there were a number of smaller anomalous areas, the population in polar areas was not significantly different from the population in a control area—Sinus Iridium, at latitude 47°N. Lunar libration was slightly more favorable when Arecibo viewed the South Pole ($\theta_i = 83.9°$) than was the case for Clementine ($\theta_i = 85.6°$). Hence, more 'ice' should have been exposed to the Arecibo radar. But, lacking any evidence for a distinctly different scattering process in the polar region, *Stacy et al.* concluded that "very rough surfaces rather than ice deposits are responsible" for the anomalous pixels in their images.

Our geometrical calculations indicated that 1.53 Hz Doppler bins near the South Pole would have 'horseshoe' shapes—approximately 500 km of arc by 8 km in width (Figure 4f and accompanying text). Near t_0 the Doppler sensitivity to vertical relief around the South Pole is about 1.37 mHz/m; if the South Pole were 1.1 km higher than our assumed 1737.4 km spherical reference, for example, it would appear in the power spectrum 1.53 Hz (one frequency bin) above the predicted location (bold lines in Figure 10). Our observation of echo power at frequencies above the nominal South Pole near $t_0 - 600$ is consistent with variability in existing models for the topography [*Smith and Zuber*, 1997]; in fact, the apparent retreat of this higher frequency scatter after $t_0 - 500$ may indicate our detection of negative topography on the edges of the South Pole Aitken Basin. But the topography model of *Smith et al.* [1997] shows a polar radius about 1.4 km smaller than our sphere, implying that we have overestimated the frequency of the South Pole by perhaps 1-2 bins. A more detailed consideration of distortions and shifts in the horseshoe-shaped 'footprints' must await new topographic data, such as are being collected by *Margot et al.* [1997].

For a Lambertian scattering function with coefficient $K_D = 0.001$, the RCP radar cross section of a 500 km by 8 km horseshoe target would be $\sigma = 4\Psi$ km^2. where Ψ is an effective value for $\cos\theta_i\cos\theta_i$ averaged over the horseshoe. A 1 dB increase would raise this to about 5Ψ km^2—equivalent to adding 1Ψ km^2 of scattering cross section to the target if the new area had $K_D{\sim}1$, a value we take to be representative of clean ice. Lower values of K_D could be assumed for the ice, but at a corresponding increase in the required areal coverage. Lower values of K_D could be obtained by making the ice less heterogeneous (reducing the density of internal scattering centers), by blanketing the ice with a lossy overburden, and/or by mixing lossy contaminants into the ice matrix. *Butler et al.* [1993] have estimated that a contaminant volume fraction of more than 5% would significantly reduce the ability of ice to scatter anomalously. Hence, the *Nozette et al.* claim of a 1 dB RCP enhancement implies a few meters' thickness of relatively pure ice spread over a minimum 1 km^2 in one of our horseshoe-shaped resolution cells. If the ice were impure, (partially) covered, or had $K_D < 1$, then the volume required would be proportionately greater. Since we find no 1 dB enhancement in our own analysis, this volume can be taken as an upper limit to the amount of clean ice present. In this regard, however, it must be recognized that the backscatter enhancement mechanisms operating in ice are not well understood.

To this point, we have focused on the *Nozette et al.* report of a 1 dB enhancement in RCP with no corresponding change in LCP echo strength. *A priori* there is no reason to rule out coincident enhancements in both polarizations—echoes from the icy Galilean satellites are unusually strong in both circular polarizations, though the apparent 'polarization reversal' is an undeniable, striking feature of the data [*Campbell et al.*, 1978]. We found several candidates near the South Pole in which both polarizations were enhanced. But these are not distinguished from other enhancements at more distant times and frequencies, so are much harder to attribute to polar deposits of ice. Lacking compelling evidence that these might otherwise result from ice scattering, we conclude, as did *Stacy et al.*, that the enhancements found much more likely reflect the heterogeneity in scattering properties that can be seen anywhere on the Moon.

By carefully tracking some of these spectral features as Doppler contours migrate over the lunar surface (*e.g.*, between Figure 4f and Figure fd), we may be able to localize their positions. Using quasi-specular bistatic data from Apollo 14 we 'mapped' the central peak, floor, rim, and ejecta blanket of the lunar crater Lansberg [*Simpson et al.*, 1977]. *Harmon et al.* [1982] have located scattering centers in diffuse echo spectra from Mars. The enhancement at −30 Hz in Figure 12 arises from surface on or near the first Doppler contour wholly outside the 85°S latitude circle in Figure 4f. The peak at −100 Hz could be as close to the South Pole as 78°S if located near the Clementine orbit plane—or as far away as 73°S if near the Mutual Terminator. At this stage in our analysis we are limited to general statements, but there is potential for improving the locations of these spectral features through additional work.

Our fit of a bistatic Lambertian scattering template to both polarizations near t_0 is the first result of its kind. Previous bistatic studies of planetary surfaces have been limited to analyses of quasi-specular echoes largely by resources available. Searching for enhanced backscatter can only be carried out using the 'spotlight' bistatic mode; there were few opportunities to search for enhanced backscatter until Clementine. Spotlight experiments were attempted at Mars using Viking Orbiters and at Venus using Magellan; but no detections, other than incidental quasi-specular echoes were obtained. Refinements to the Clementine scattering function will be possible by analyzing spectra from other parts of Orbit 234 and from other orbits. With more data, it will also be interesting to compare the bistatic function with functions derived from monostatic radars. Full disk studies of lunar monostatic echoes in the time domain have implied a $\cos\theta_i$ power dependence near the limb [*Hagfors and Evans*, 1968]—in agreement with our results, despite our preference for the Lambertian function when considering the full lunar disk.

6. Conclusions

The Clementine bistatic radar experiment has yielded a unique data set. Our derivation of a bistatic radar cross section for highly oblique scattering is a step toward better understanding of bistatic scattering from planetary surfaces, and the Moon's in particular. We intend to follow up on this work with a more extensive analysis of the Clementine data.

Our primary objective here was to verify, through an independent search, the enhanced backscatter signature reported by *Nozette et al.* [1996]. Although we have found many examples of enhancements in scattering in both frequency and time near the South Pole, none have the unique signature reported in the earlier study. The enhancements we did find are easily attributed to local terrain variations, including topography and changes in meter-scale surface roughness or blockiness, and do not require presence of ice. Our failure to find a distinctive ice signature corroborates the conclusions of *Stacy et al.* [1997] who found no evidence for ice-caused scattering anomalies near the South Pole when using Arecibo monostatic radar.

This negative result applies only to detection of large exposures of clean 'block' ice. A pure ice matrix is remarkable in its transmission and scattering of microwave signals; high backscatter from the icy Galilean satellites of Jupiter strongly implies that impurities are at low concentrations throughout the upper surfaces of those bodies. The *Nozette et al.* detection corresponds to 0.025% areal coverage in a single horseshoe-shaped footprint to a depth of a few meters with nearly pure ice. Since we do not find the ice signature in the Clementine data, we take these coverage estimates as upper bounds on the possible ice coverage.

Contaminants within the ice (or covering by a lossy overburden) would raise the areal fraction required—except that contaminants in volume fractions of more than a few percent will degrade the unusual scattering properties of ice to the point where it becomes indistinguishable from soil. Ice distributed uniformly through a regolith in mixing ratios under 1%, such as has been suggested by early Lunar Prospector results, would not be detected by the Clementine radar experiment.

Acknowledgments. The Clementine bistatic radar experiment was proposed by Stewart Nozette; Christopher Lichtenberg served as principal investigator during its execution. Without their participation, no experiment would have been performed. Within the Jet Propulsion Laboratory and Deep Space Network the assistance of Sami Asmar, Sal Abbate, and Ann Devereaux was critical to collection of the data. At Stanford Nejat Cingi assisted with development of analysis software. Data have been archived with the Planetary Data System; this analysis constituted part of its PDS peer review. This work was supported through the Lunar and Asteroid Data Analysis Program under grant NAGW 4878.

References

Campbell, D.B., J.F. Chandler, S.J. Ostro, G.H. Pettengill, and I.I. Shapiro, Galilean satellites: 1976 radar results, *Icarus*, *34*, 254-267, 1978.

Hagfors, T., and J.V. Evans, Radar studies of the Moon, in *Radar Astronomy*, edited by J.V. Evans and T. Hagfors, pp 219-273, McGraw-Hill, New York, 1968.

Hapke, B., and D. Blewett, Coherent backscatter model for the unusual radar reflectivity of icy satellites, *Nature*, *352*, 46-47, 1991.

Harmon, J.K., D.B. Campbell, and S.J. Ostro, Dual-polarization radar observations of Mars: Tharsis and environs, *Icarus*, *52*, 171-187, 1982.

Margot, J.L., D.B. Campbell, R.F. Jurgens, M.A. Slade, and N.J. Stacy, High resolution topographic maps of the lunar south pole, *Bull. AAS*, *29*, 986, 1997.

Muhleman, D.O., A.W. Grossman, and B.J. Butler, Radar investigations of Mars, Mercury, and Titan, *Annual Reviews of Earth and Planetary Science*, *23*, 337-374, 1995.

Nozette, S., C.L. Lichtenberg, P. Spudis, R. Bonner, W. Ort, E. Malaret, M. Robinson, E.M. Shoemaker, The Clementine bistatic radar experiment, *Science*, *274*, 1495-1498, 1996.

Smith, D.E., and M.T. Zuber, Topography of the lunar South Pole region: implications for the location and distribution of permanently shaded areas, paper presented at Lunar and Planetary Science Conference XXVIII, Houston, 1997.

Smith, D.E., M.T. Zuber, G.A. Neumann, and F.G. Lemoine, Topography of the Moon from the Clementine lidar, *J. Geophys. Res.*, *102*, 1591-1611, 1997.

Simpson, R.A., Spacecraft studies of planetary surfaces using bistatic radar, *IEEE Transactions, GRS-31*, 465-482, 1993.

Simpson, R.A., G.L. Tyler, and H.T. Howard, Crater morphometry from bistatic radar, in *Impact and Explosion Cratering*, edited by D.J. Roddy, R.O. Pepin, and R.B. Merrill, pp 481-487, Pergamon, New York, 1977.

Stacy, N.J.S., D.B. Campbell, and P.G. Ford, Arecibo radar mapping of the lunar poles: a search for ice deposits, *Science*, *276*, 1527-1530, 1997.

Tyler, G.L., Radio propagation experiments in the outer solar system with Voyager, *Proceedings of the IEEE*, *75*, 1404-1431, 1987.

Figure Captions

Figure 1. Geometry for Clementine bistatic radar. Vectors from the South Pole target to the transmitter and receiver are $\mathbf{t_{sp}}$ and $\mathbf{r_{sp}}$, respectively; they are not necessarily in the orbit plane but must be close to the plane for near-backscatter observations of the Pole. Arrows show bistatic propagation path. Bistatic angle β_{sp} is the angular separation between transmitter and receiver when viewed from the Pole.

Figure 2. Ground track for $\beta=0°$ point on Clementine orbit 234. Earth is toward the top; the Moon's planetographic east limb is to the right. Dashed lines indicate circles of constant latitude in 1° steps away from the South Pole. Points are spaced in time by one second. The time when an Earth-based observer saw the $\beta=0°$ track pass closest to the Pole was approximately 67596.5 sec at a distance of about 3.5 km; the last $\beta=0°$ point on the disk was at 67603 sec.

Figure 3. Incidence (θ_i), scattering (θ_s), and bistatic (β) angles for South Pole target as a function of time on Clementine orbit 234. Minimum β for the Pole was about 0.1°, at which time $\theta_i = \theta_s = 85.61°$.

Figure 4. Contour plots of key observational parameters at t_0—the time when β was minimum for the South Pole. View is vertically down on the South Pole ('+') with Earth and Clementine both toward the top (+X) and the lunar planetographic east limb to the right (+Y). Dashed lines are circles of constant latitude in 5° steps; the only complete circle shown is for 85°S. Computational grid had 700x700 points, spaced by 5 km each. (a) Incidence angle contours, starting at 90° and decreasing in 5° steps toward the top. 90° contour defines the horizon as seen from the spacecraft; the 60° contour is labeled. (b) Scattering angle contours, also from 90° in –5° steps. 90° contour defines the limb seen from Earth-based receiving antenna; the 85° contour is labeled. (c) Bistatic angle contours starting from $\beta=1°$ and working outward in +1° steps. (d)

Transmit antenna gain from 25 dBi in steps of –5 dB outward to –5 dBi, then rising to +5 dBi for the first sidelobe before dropping again. Peak gain near the South Pole was 26.2 dBi. (e) Receive antenna gain from 62 dBi in steps of –2 dB outward; boresight gain was 63.2 dBi. (f) Echo intensity per unit surface area (elliptical contours, truncated by mutual transmit-receive terminator) overlying contours of Doppler offset (approximate circles). Intensity was calculated using the radar equation (1) for each grid element assuming $\sigma_0 = 1$; contour interval is 5 10^{-20} watts. Doppler bins are 12.2 Hz wide with the South Pole centered in the next-to-highest bin.

Figure 5. Contours of bistatic angle (a) and echo intensity overlying Doppler offset (b) calculated for a time 500 seconds before t_0 (compare with Figure 4c and 4f). The $\beta=1°$ contour is at 55°S latitude; the South Pole is beyond the spacecraft horizon. Echo intensity contours were calculated assuming $\sigma_0 = 1$ and are spaced by 5 10^{-20} watts; Doppler contours are spaced by 12.2 Hz. Contours of bistatic angle (c) and echo intensity overlying Doppler offset (d) calculated 300 seconds after t_0.

Figure 6. (a) Simplified block diagram for receiving and recording at the NASA DSN station. Equivalent chains operated in parallel for right- and left-circular polarization. The programmable oscillator was driven from a file of predicted frequencies and linear drifts. Following the second mixer were several stages of down-conversion and amplification (not shown). The filter was centered at 10 MHz and had a 3 dB width of 21 kHz. Real 8-bit samples were taken at a rate of 50000 per second from each polarization, merged, and written to digital tape. (b) Simplified diagram showing data processing at Stanford. Samples were parsed from tape into separate streams for RCP and LCP; only RCP is shown here. Samples were scaled for correct amplitude against a known standard. In two steps, phase of samples was adjusted so that frequency corresponding to the South Pole would be at exactly 12.5 kHz. f_c and f_{sp} are carrier frequency and South Pole frequency in baseband output, respectively. Digital bandpass filtering allowed extraction of noise statistics. Functions at each stage are described more fully in the text.

Figure 7. Power versus time for both RCP (upper) and LCP (lower) computed from raw data samples (1 sec averages). The RCP curve has been raised by 6 dB to facilitate display. Long-period fluctuations (minutes) result from changes in sidelobe radiation from the back of the spacecraft high-gain antenna and from changes in bulk scattering from the lunar surface. Events A-F, based on examination at high time resolution, are 1 dB attenuator changes in the receiving systems; most can be confirmed from header entries in data records. Event G appears to have been a spontaneous 0.7 dB maser or amplifier gain change (see text). Events B, F, and G are within 40 sec of t_0.

Figure 8. Power spectra from raw data samples around t_0. Individual spectra were computed from 1024 real samples, representing 25 kHz, and were then summed incoherently over approximately 60 seconds. The 16 spectra shown here cover 67005 to 67965 secs. The narrow carrier signal reaching Earth from sidelobes of the spacecraft high-gain antenna drifts toward lower frequencies; the lunar echo, dispersed in frequency from multiple surface interactions, drifts toward higher frequencies. The sharp drop on the high-frequency end of the echo spectrum marks the mutual transmitter/receiver terminator.

Figure 9. Frequency estimates for the Clementine carrier after phase of RCP time samples was adjusted by a piecewise linear fit to one second frequency averages. Remaining fluctuations (0.9253 Hz rms about the 12.5 kHz mean) are believed to reflect instabilities in the spacecraft oscillator.

Figure 10. High resolution plots of 22 individual spectral bins near the time of South Pole backscatter for RCP (a) and LCP (b). Points have been smoothed with a 100 second running average (153-point 'boxcar'). Bold line shows time variability of bin associated with the South Pole. Bins are separated by 1.53 Hz from 13.73 Hz above the Pole frequency (bottom) to 18.31

Hz below the Pole frequency (top). Points in the lower left of each panel contain only radiothermal noise from the Moon (Doppler shift is too high for a radar echo). Best candidates for enhanced echoes near t_0 are 8 and 12 bins above the bold line (Doppler offsets of −12.21 and −18.31 Hz); but each 'enhancement' appears in both polarizations.

Figure 11. Predicted bistatic echo power spectra for four assumed specific radar cross sections at t_0. (A) $\sigma_0 = K_A = 0.05$. (B) $\sigma_0 = K_B \cos\theta_i$ with $K_B = 1/3$. (C) $\sigma_0 = K_C \cos\theta_s$ with $K_C = 1/3$. (D) $\sigma_0 = K_D \cos\theta_i \cos\theta_s$ with $K_D = 1$.

Figure 12. LCP and RCP echo spectra at the time of South Pole backscatter. Both data curves are 100 sec averages centered on t_0. Smooth curves are least-square-error best fits to amplitude of a Lambertian template calculated numerically. Best fit coefficients and rms errors are shown in the figure.

Table 1. Sensitivity Comparison

	Symbol	Arecibo Monostatic	Clementine Bistatic
Transmitted Power	P_T	450 kw	7.1 w
Transmitting Antenna Boresight Gain	$G_T(\theta_T{=}0°)$	73 dB	26.2 dB
Transmitter Distance	$\lvert t\rvert$	$\sim 4 \cdot 10^8$ m	$\sim 4 \cdot 10^6$ m
Target Radar Cross Section	$\sigma = \sigma_0(\theta_i,\theta_s,\beta)\ dA(f)$	$\sigma = \sigma_0\ dA$	$\sigma = \sigma_0\ dA$
Wavelength	λ	0.126 m	0.132 m
Receiving Antenna Boresight Gain	$G_R(\theta_R{=}0°)$	73 dB	63.22 dB
Receiving Antenna Aperture	$A_R = \frac{\lambda^2 G_R}{4\pi}$	25207 m^2	2910 m^2
Receiver Distance	$\lvert r\rvert$	$\sim 4 \cdot 10^8$ m	$\sim 4 \cdot 10^8$ m
Received Power (radar equation)	$P_R = \frac{P_T G_T}{4\pi\lvert t\rvert^2}\,\sigma\,\frac{A_R}{4\pi\lvert r\rvert^2}$	$\sim 5.6 \cdot 10^{-20}\ \sigma$	$\sim 2.7 \cdot 10^{-25}\ \sigma$
Transmit antenna, off-boresight angle	θ_T		
Receive antenna, off-boresight angle	θ_R		
Surface element, incidence angle	θ_i		
Surface element, scattering angle	θ_s		
Bistatic angle	β		

Table 2. Amplitude Calibration Measurements

No	Target	Start (sec)	Stop (sec)	Number of Points	Attenuator (dB)	Mean±Standard Deviation Measured Noise Power (linear)	Adjusted Mean (linear)	Weighted Average (linear)
R01	SKY	64150	64675	526	30.00	4.455e-03±8.101e-05	4.455	4.455
R02	AMB	64695	64745	51	39.80	6.679e-03±1.333e-04	63.785	63.606[1]
R03	AMB	64760	64875	116	40.80	5.284e-03±9.526e-05	63.528	
R04	LIM	65562	65612	51	39.80	1.735e-03±3.426e-05	16.568	
R05	LIM	65614	65790	177	35.00	5.079e-03±1.011e-04	16.061	
R06	LIM	65793	65887	95	39.80	1.737e-03±3.332e-05	16.592	
R07	LIM	65891	66045	155	38.00	2.547e-03±5.492e-05	16.072	
R08	LIM	66046	67005	960	38.00	2.521e-03±5.824e-05	15.905	
R09	LIM	67006	67235	230	38.00	2.475e-03±4.463e-05	15.618	16.014[2]
R10	LIM	67239	67557	319	39.00	1.940e-03±4.515e-05	15.414	
R11	LIM	67561	67965	405	39.80	1.676e-03±3.670e-05	16.010	
R12	LIM	67966	68925	960	39.80	1.671e-03±3.855e-05	15.959	
R13	LIM	68926	69885	960	39.80	1.660e-03±3.777e-05	15.851	
R14	LIM	69886	70845	960	39.80	1.701e-03±3.573e-05	16.249	
R15	LIM	70846	71460	615	39.80	1.723e-03±3.675e-05	16.456	
R16	CTR	71489	71522	34	35.00	1.301e-02±3.014e-04	41.138	42.330[3]
R17	CTR	71525	71700	176	39.80	4.457e-03±8.637e-05	42.560	
R18	AMB	71745	71805	61	39.80	6.352e-03±9.985e-05	60.664	60.298[4]
R19	AMB	71815	72105	291	40.80	5.009e-03±9.075e-05	60.221	
R20	SKY	72125	72309	185	30.00	4.212e-03±7.620e-05	4.212	4.212
L01	SKY	64175	64675	501	30.00	2.202e-03±4.098e-05	2.202	2.202
L02	AMB	64685	64765	81	40.00	3.337e-03±8.062e-05	33.373	33.436[5]
L03	AMB	64770	64870	101	41.00	2.660e-03±6.021e-05	33.486	
L04	LIM	65571	65605	35	40.00	9.865e-04±2.184e-05	9.865	
L05	LIM	65607	65815	209	35.00	3.078e-03±6.549e-05	9.733	
L06	LIM	65819	65885	67	40.00	9.781e-04±1.846e-05	9.781	
L07	LIM	65888	66045	158	38.00	1.522e-03±3.029e-05	9.602	
L08	LIM	66046	67005	960	38.00	1.513e-03±3.376e-05	9.545	
L09	LIM	67006	67239	234	38.00	1.507e-03±2.905e-05	9.505	
L10	LIM	67243	67290	48	39.00	1.175e-03±2.518e-05	9.332	
L11	LIM	67292	67350	59	40.00	9.465e-04±2.017e-05	9.465	9.543[6]
L12	LIM	67353	67552	200	41.00	7.639e-04±1.921e-05	9.617	
L13	LIM	67555	67558	4	42.00	6.247e-04±8.386e-06	9.900	
L14	LIM	67565	67965	401	42.70	5.253e-04±1.113e-05	9.782	
L15	LIM	67966	68445	480	42.70	5.193e-04±1.177e-05	9.669	
L16	LIM	68926	68935	10	42.70	5.229e-04±9.387e-06	9.736	
L17	LIM	69886	70845	960	42.00	5.922e-04±1.269e-05	9.386	
L18	LIM	70846	71460	615	42.00	5.942e-04±1.282e-05	9.417	
L19	CTR	71610	71710	101	35.00	6.896e-03±1.441e-04	21.808	21.808
L20	AMB	71745	71800	56	35.00	9.889e-03±1.854e-04	31.273	31.488[7]
L21	AMB	71806	72105	300	41.00	2.504e-03±4.567e-05	31.528	
L22	SKY	72125	72309	185	30.00	2.083e-03±3.885e-05	2.083	2.083

(continued)

Measurements Rnn are for RCP; Lnn are for LCP. Targets are: AMB = ambient load; CTR = center of Moon; LIM = South Pole and lunar limb; and SKY = dark sky. Each 'point' is a 1-sec average power taken from band-limited noise samples (no direct signal or echo). Measured mean (column 7), scaled by attenuator setting (column 6), gives adjusted mean (column 8); non-integer attenuator settings are explained in text. Weighted average (column 9) gives average measured noise level from several intervals—*e.g.*, with different attenuator settings. Averaging intervals are given by superscripts:

[1] R02 and R03

2 R04 through R15

[3] R16 and R17

[4] R18 and R19

[5] L02 and L03

[6] L04 through L18

[7] L20 and L21

Values in column 9 were used in equations (4)-(6) to find T_{sys}, T_{ctr}, and T_{lim}.

Table 3. Equivalent Noise Temperatures from Calibration Measurements

Right Circular (RCP) Polarization

T_{sky} (K)	T_{sys} (K) (64150-64875 s) (Y_1=14.28)	T_{sys} (K) (71745-72309 s) (Y_1=14.32)	T_{ctr} (K) (71489-72105 s) (Y_2=1.424)	T_{lim} (K) (65562-72105 s) (Y_3=3.765)
0	21.65	21.59	195.35	59.06
1	20.57	20.51	195.67	59.86
3	18.42	18.36	196.31	61.45
5	16.27	16.21	196.96	63.40

Left Circular (LCP) Polarization

T_{sky} (K)	T_{sys} (K) (64150-64875 s) (Y_1=15.18)	T_{sys} (K) (71745-72309 s) (Y_1=15.12)	T_{ctr} (K) (71610-72105 s) (Y_2=1.444)	T_{lim} (K) (65571-72105 s) (Y_3=3.300)
0	20.26	20.36	192.82	72.92
1	19.19	19.29	193.15	73.67
3	17.05	17.15	193.81	75.16
5	14.91	15.01	194.47	76.66

Table 4. Scattering Functions

Label (Fig. 11)	Name (if any)	Functional Form	Best Fit Values (18:45:46-18:47:27)	
			RCP	LCP
A	Constant	$\sigma_0 = K_A$	N/A	N/A
B	Incident Cosine	$\sigma_0 = K_B\cos(\theta_i)$	$K_B = 0.000358$	$K_B = 0.001120$
C	Scattering Cosine	$\sigma_0 = K_C\cos(\theta_s)$	$K_C = 0.000376$	$K_C = 0.001172$
D	Lambertian	$\sigma_0 = K_D\cos(\theta_i)\cos(\theta_s)$	$K_D = 0.001039$	$K_D = 0.003325$

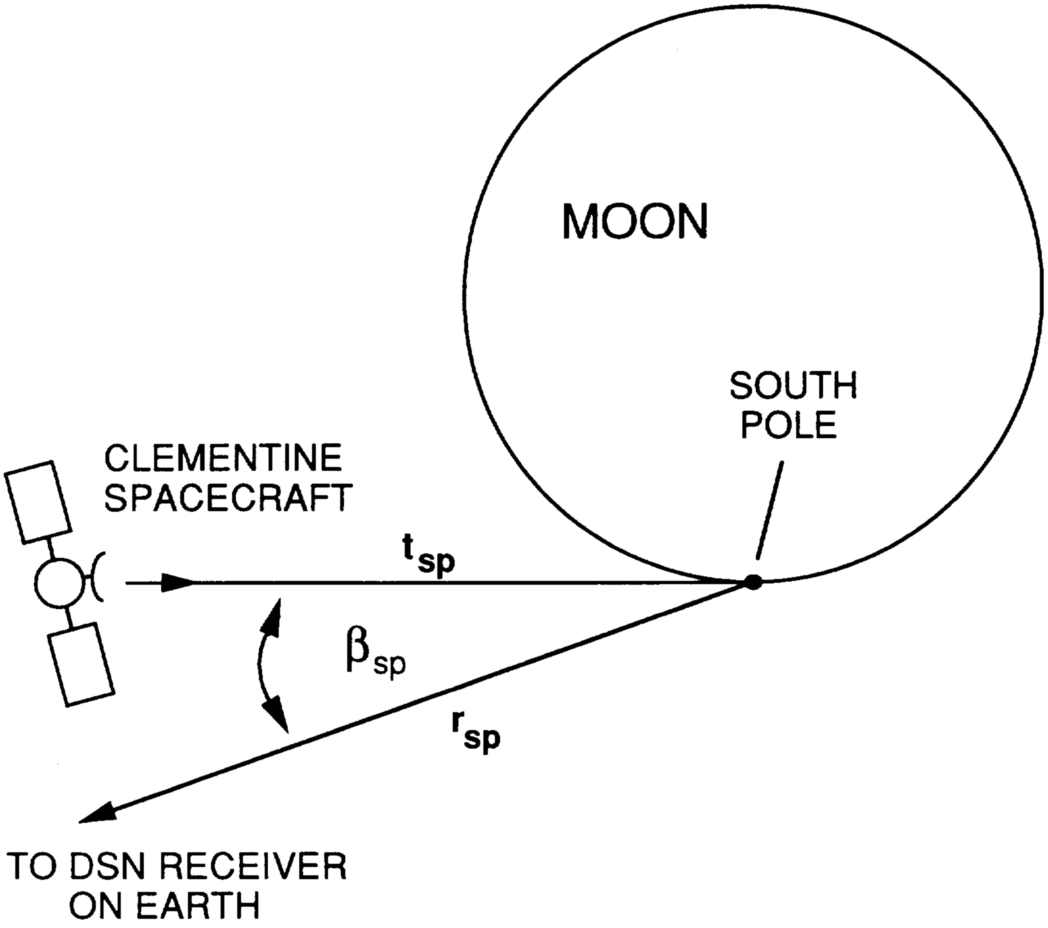
MOON
SOUTH POLE
CLEMENTINE SPACECRAFT
t_{sp}
β_{sp}
r_{sp}
TO DSN RECEIVER ON EARTH

Figure 1

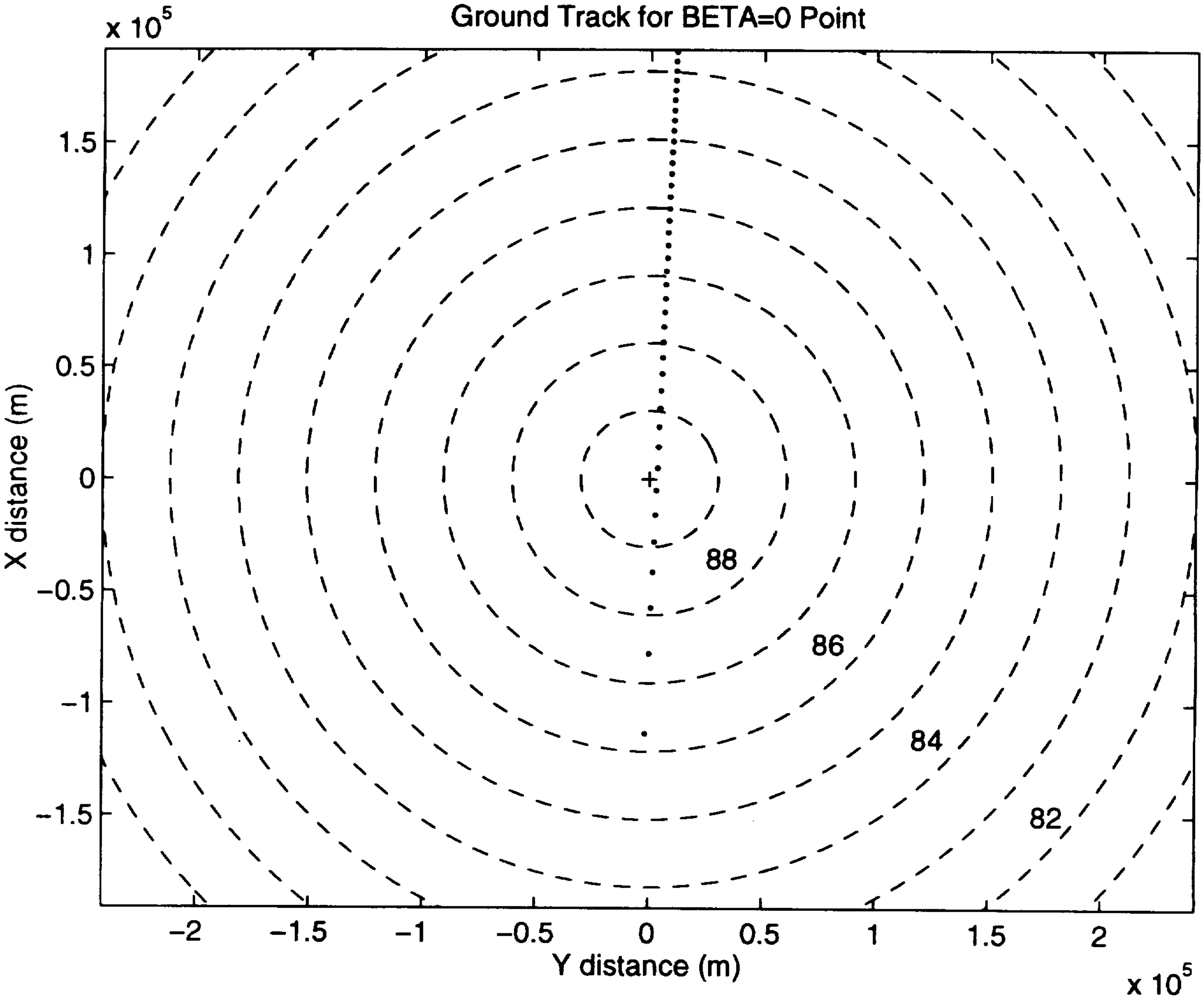

Ground Track for BETA=0 Point
x 10^5
1.5
1
0.5
0
−0.5
−1
−1.5
X distance (m)
88
86
84
82
−2
−1.5
−1
−0.5
0
0.5
1
1.5
2
Y distance (m)
x 10^5

FIGURE 2

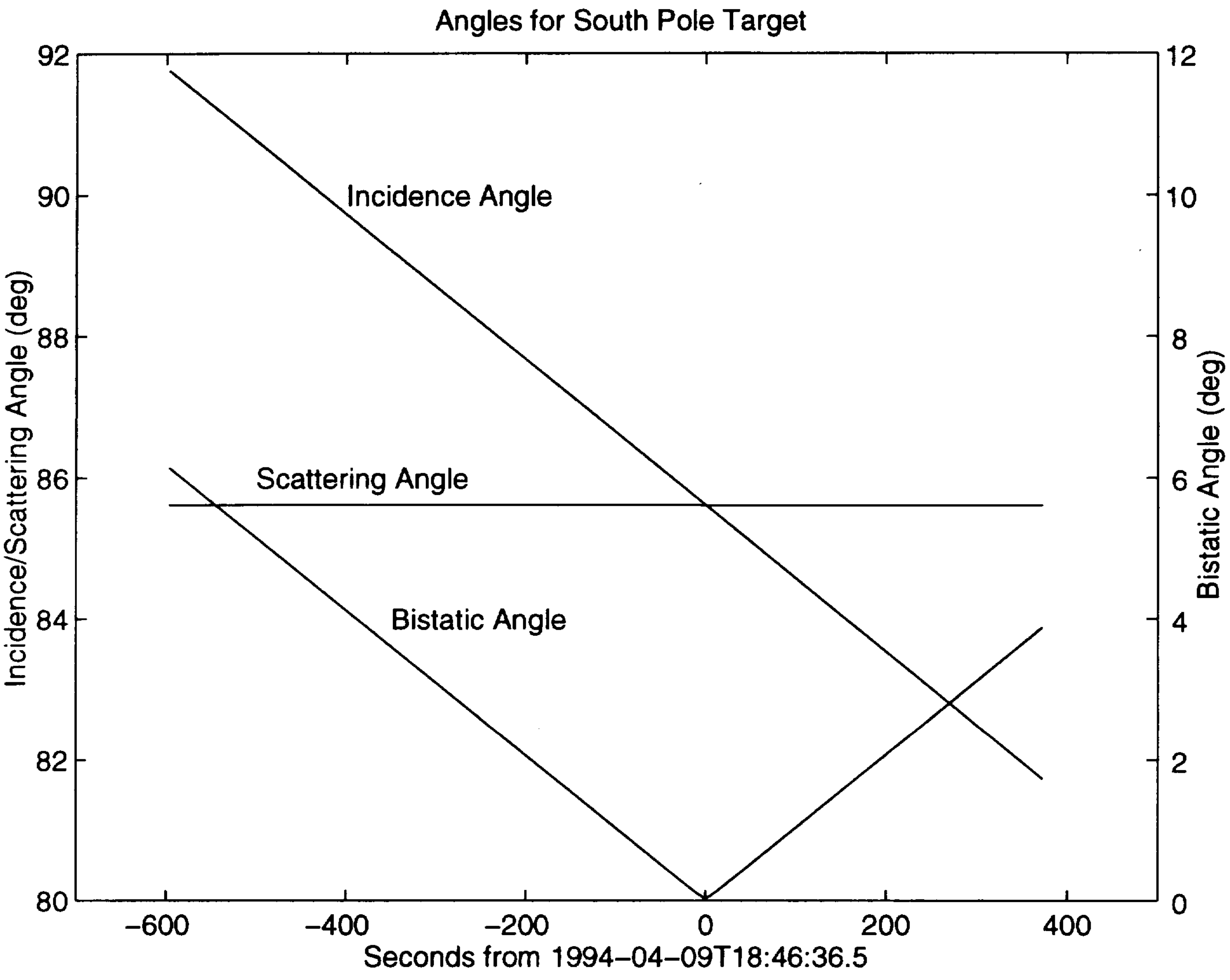

Angles for South Pole Target
Incidence Angle
Scattering Angle
Bistatic Angle
Incidence/Scattering Angle (deg)
Bistatic Angle (deg)
92
90
88
86
84
82
80
12
10
8
6
4
2
0
-600
-400
-200
0
200
400
Seconds from 1994-04-09T18:46:36.5

FIGURE 3

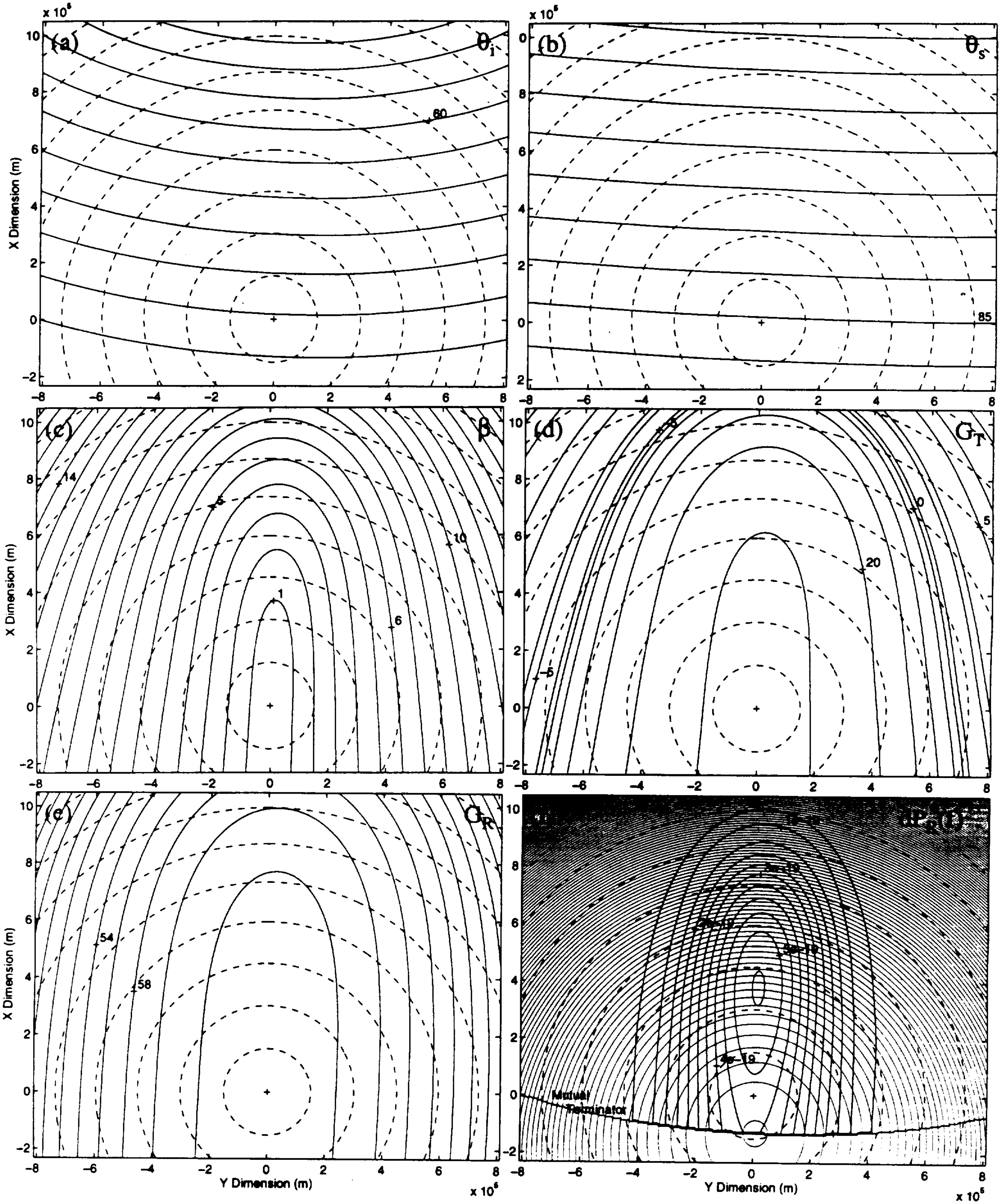
(a)
θ_i
60
(b)
θ_S
85
(c)
β
14
5
10
1
6
(d)
G_T
0
5
20
-5
(e)
G_R
54
58
dP_R(t)
1e-19
3e-19
2e-19
5e-19
4e-19
Mutual
Terminator
x 10^5
X Dimension (m)
Y Dimension (m)
-8
-6
-4
-2
0
2
4
6
8
10

FIGURE 4

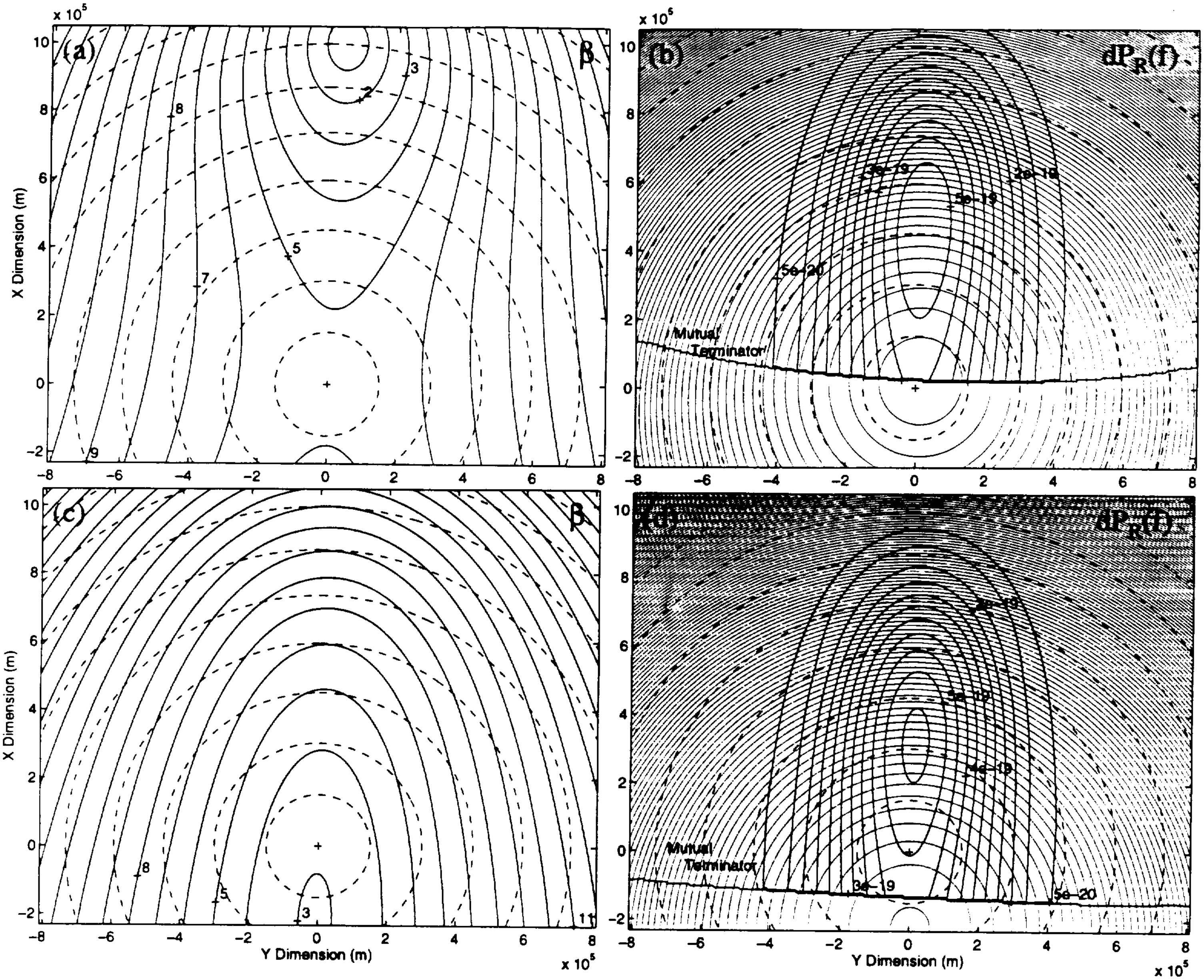
(a)
β
(b)
dP_R(f)
(c)
β
(d)
dP_R(f)
x 10^5
X Dimension (m)
Y Dimension (m)
3
2
8
5
7
9
3e-19
2e-19
5e-19
5e-20
Mutual Terminator
8
5
3
11
2e-19
5e-19
4e-19
3e-19
5e-20
-8 -6 -4 -2 0 2 4 6 8
-2 0 2 4 6 8 10

FIGURE 5

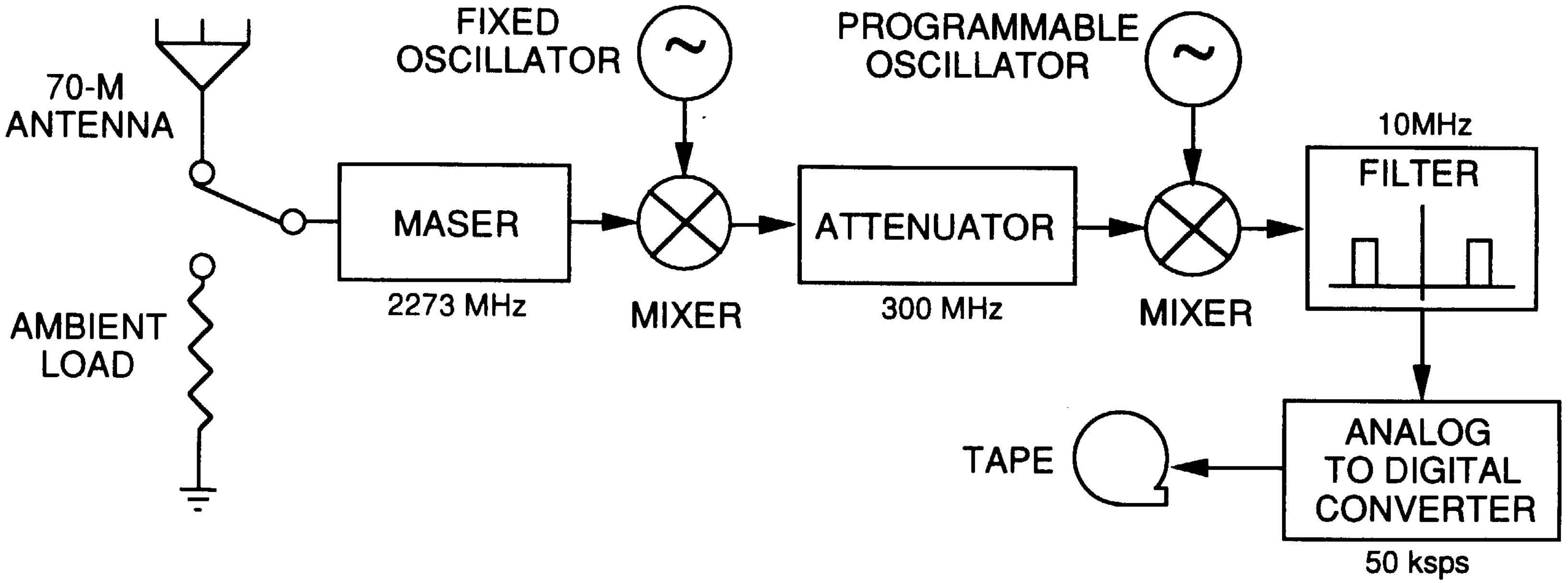
70-M
ANTENNA
AMBIENT
LOAD
MASER
2273 MHz
FIXED
OSCILLATOR
MIXER
ATTENUATOR
300 MHz
PROGRAMMABLE
OSCILLATOR
MIXER
10MHz
FILTER
ANALOG
TO DIGITAL
CONVERTER
50 ksps
TAPE

Figure 6a

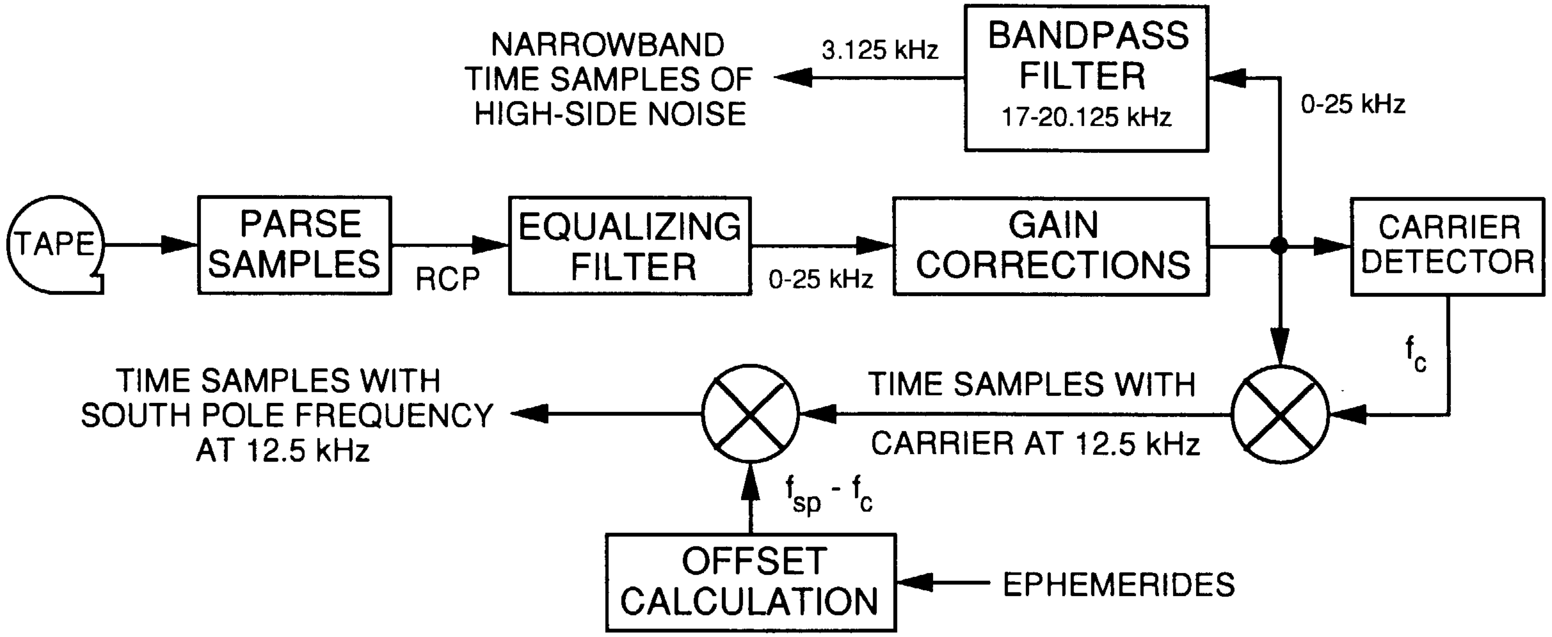
NARROWBAND
TIME SAMPLES OF
HIGH-SIDE NOISE
3.125 kHz
BANDPASS
FILTER
17-20.125 kHz
0-25 kHz
TAPE
PARSE
SAMPLES
RCP
EQUALIZING
FILTER
0-25 kHz
GAIN
CORRECTIONS
CARRIER
DETECTOR
f_c
TIME SAMPLES WITH
SOUTH POLE FREQUENCY
AT 12.5 kHz
TIME SAMPLES WITH
CARRIER AT 12.5 kHz
$f_{sp} - f_c$
OFFSET
CALCULATION
EPHEMERIDES

Figure 6b

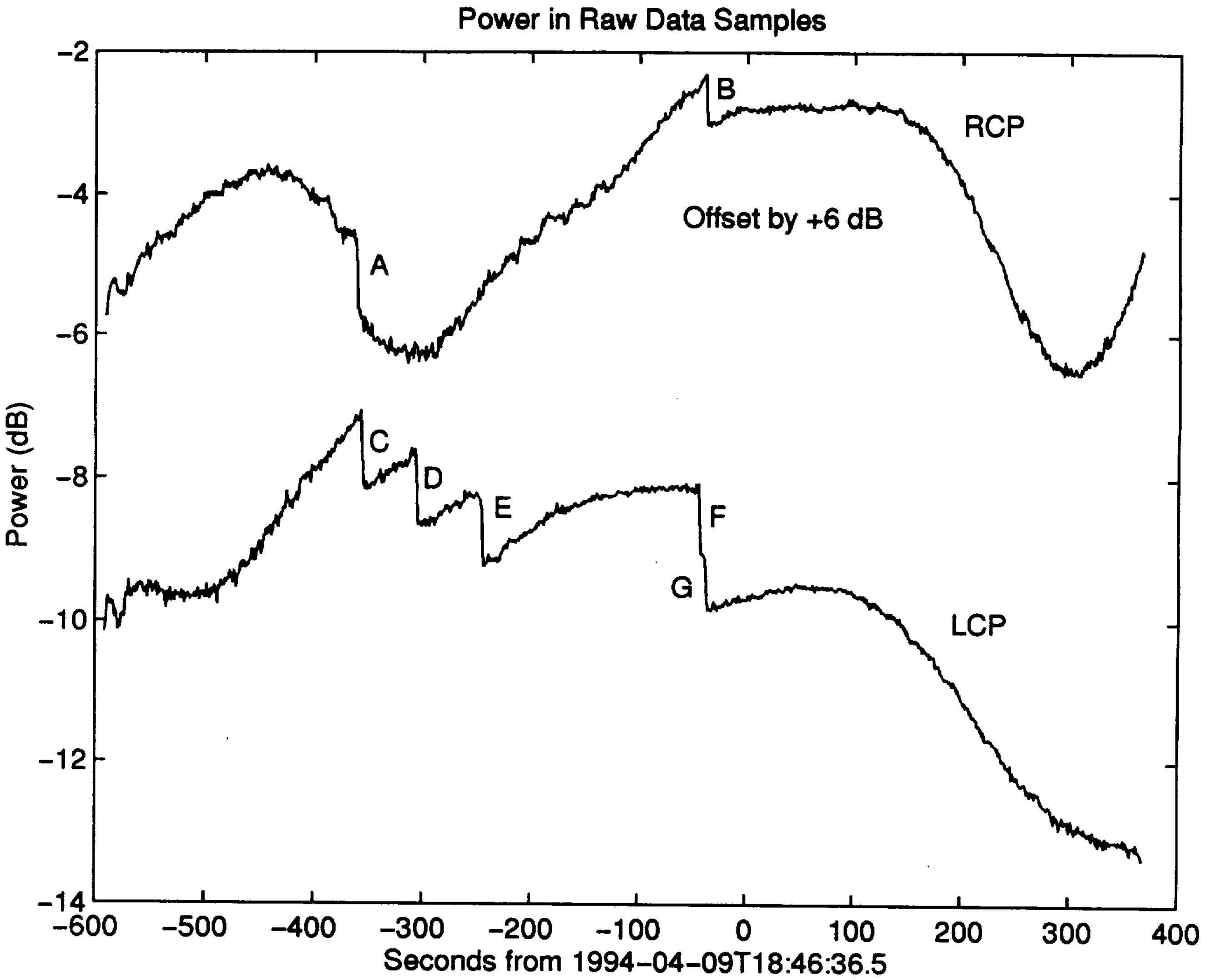
Power in Raw Data Samples
Power (dB)
-2
-4
-6
-8
-10
-12
-14
-600
-500
-400
-300
-200
-100
0
100
200
300
400
Seconds from 1994-04-09T18:46:36.5
A
B
RCP
Offset by +6 dB
C
D
E
F
G
LCP

FIGURE 7

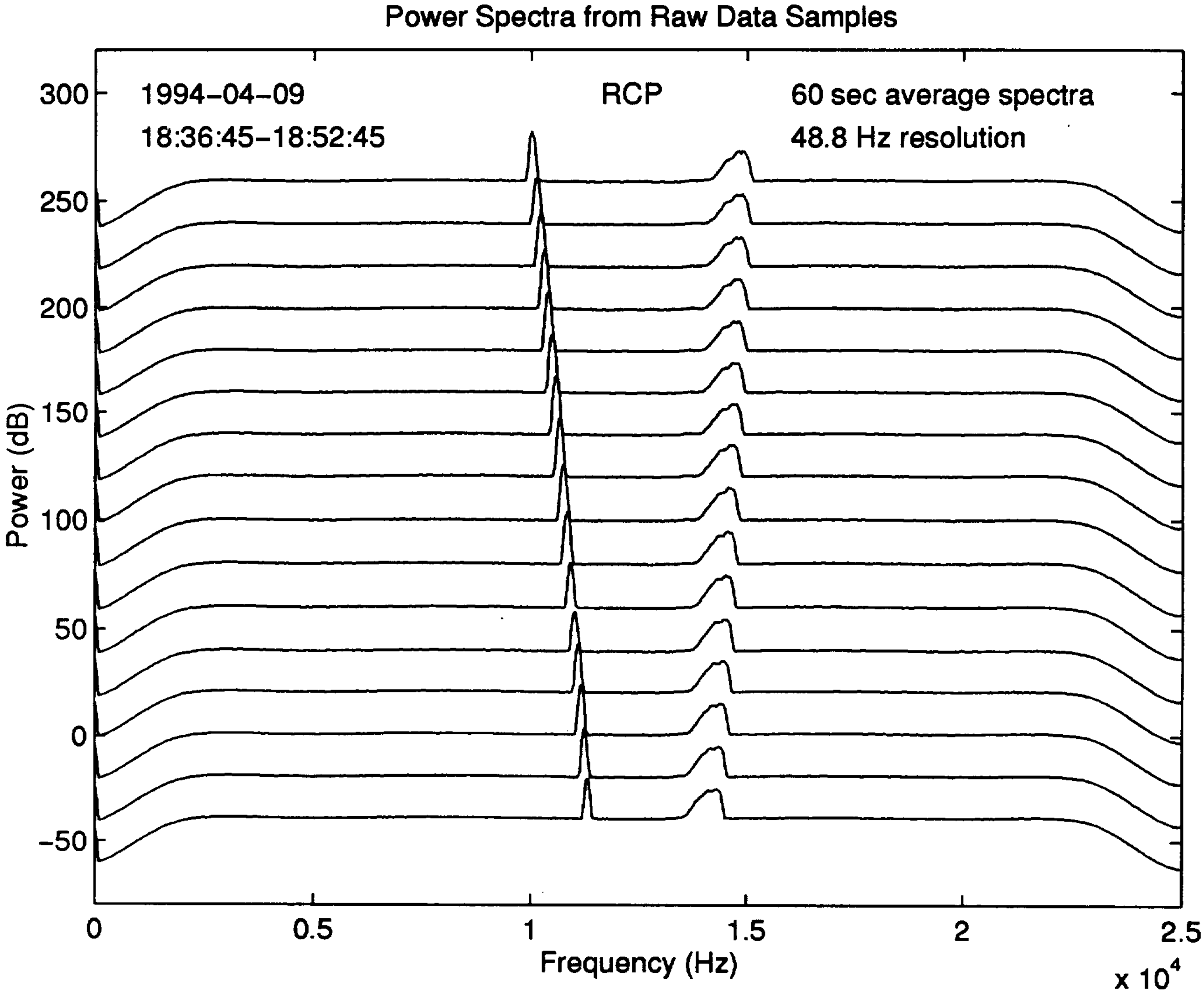
Power Spectra from Raw Data Samples
1994-04-09
18:36:45-18:52:45
RCP
60 sec average spectra
48.8 Hz resolution
Power (dB)
300
250
200
150
100
50
0
-50
0
0.5
1
1.5
2
2.5
Frequency (Hz)
x 10^4

Figure 8

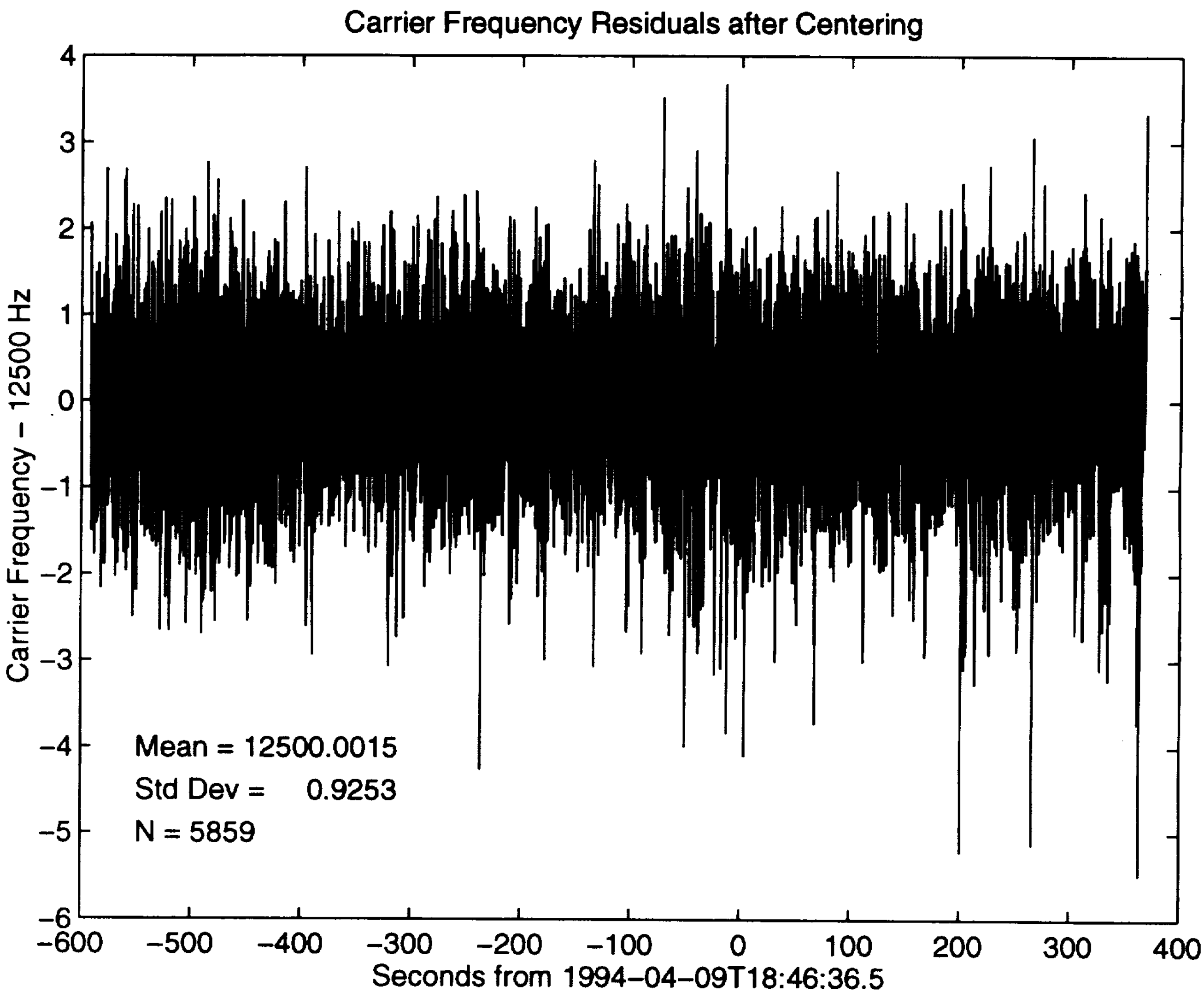
Carrier Frequency Residuals after Centering
Carrier Frequency - 12500 Hz
Seconds from 1994-04-09T18:46:36.5
4
3
2
1
0
-1
-2
-3
-4
-5
-6
-600
-500
-400
-300
-200
-100
0
100
200
300
400
Mean = 12500.0015
Std Dev = 0.9253
N = 5859

FIGURE 9

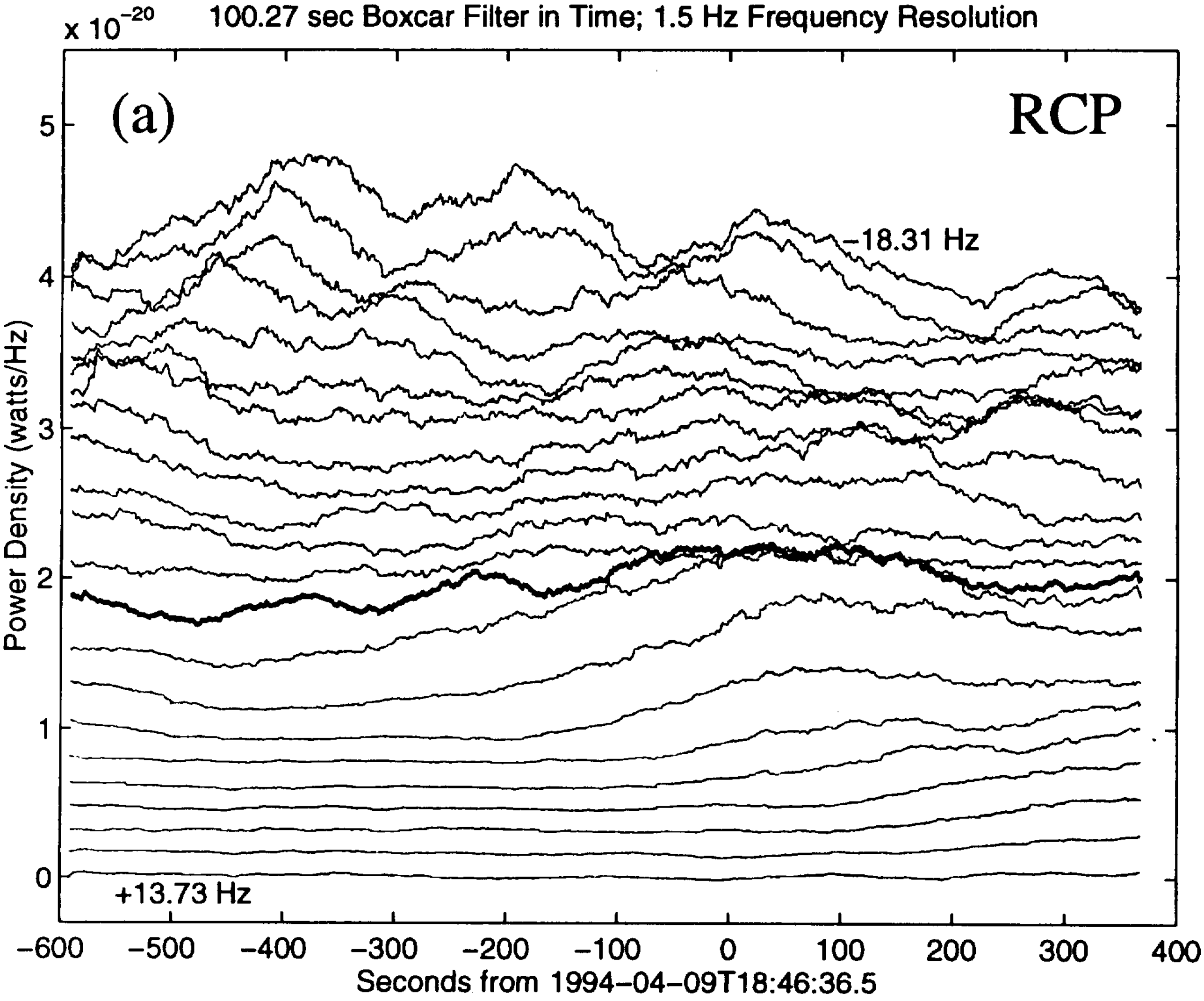
x 10^{-20}
100.27 sec Boxcar Filter in Time; 1.5 Hz Frequency Resolution
(a)
RCP
-18.31 Hz
+13.73 Hz
Power Density (watts/Hz)
0
1
2
3
4
5
-600
-500
-400
-300
-200
-100
0
100
200
300
400
Seconds from 1994-04-09T18:46:36.5

FIGURE 10a

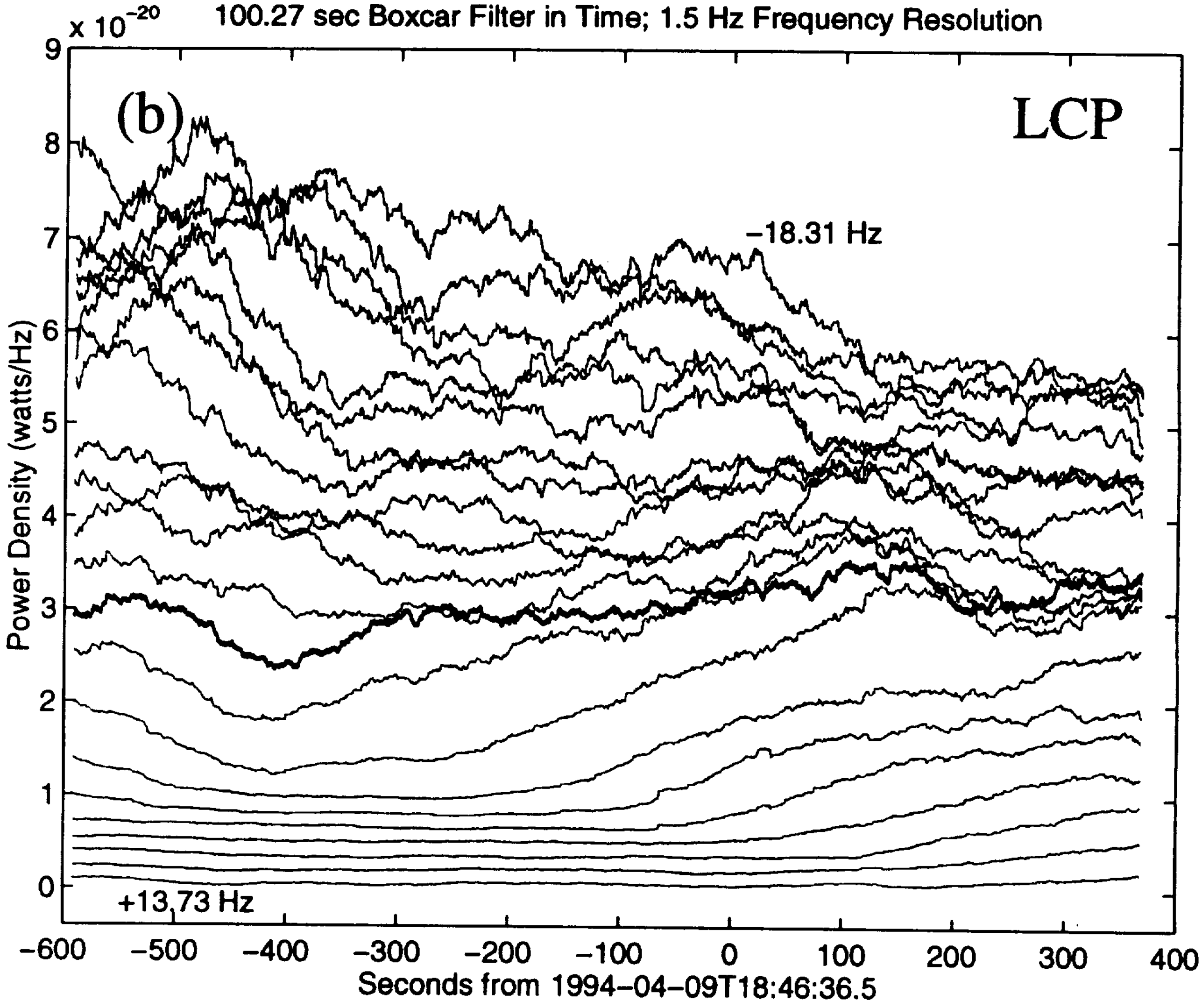
x 10^-20
100.27 sec Boxcar Filter in Time; 1.5 Hz Frequency Resolution
(b)
LCP
−18.31 Hz
+13.73 Hz
Power Density (watts/Hz)
9
8
7
6
5
4
3
2
1
0
−600
−500
−400
−300
−200
−100
0
100
200
300
400
Seconds from 1994−04−09T18:46:36.5

FIGURE 10b

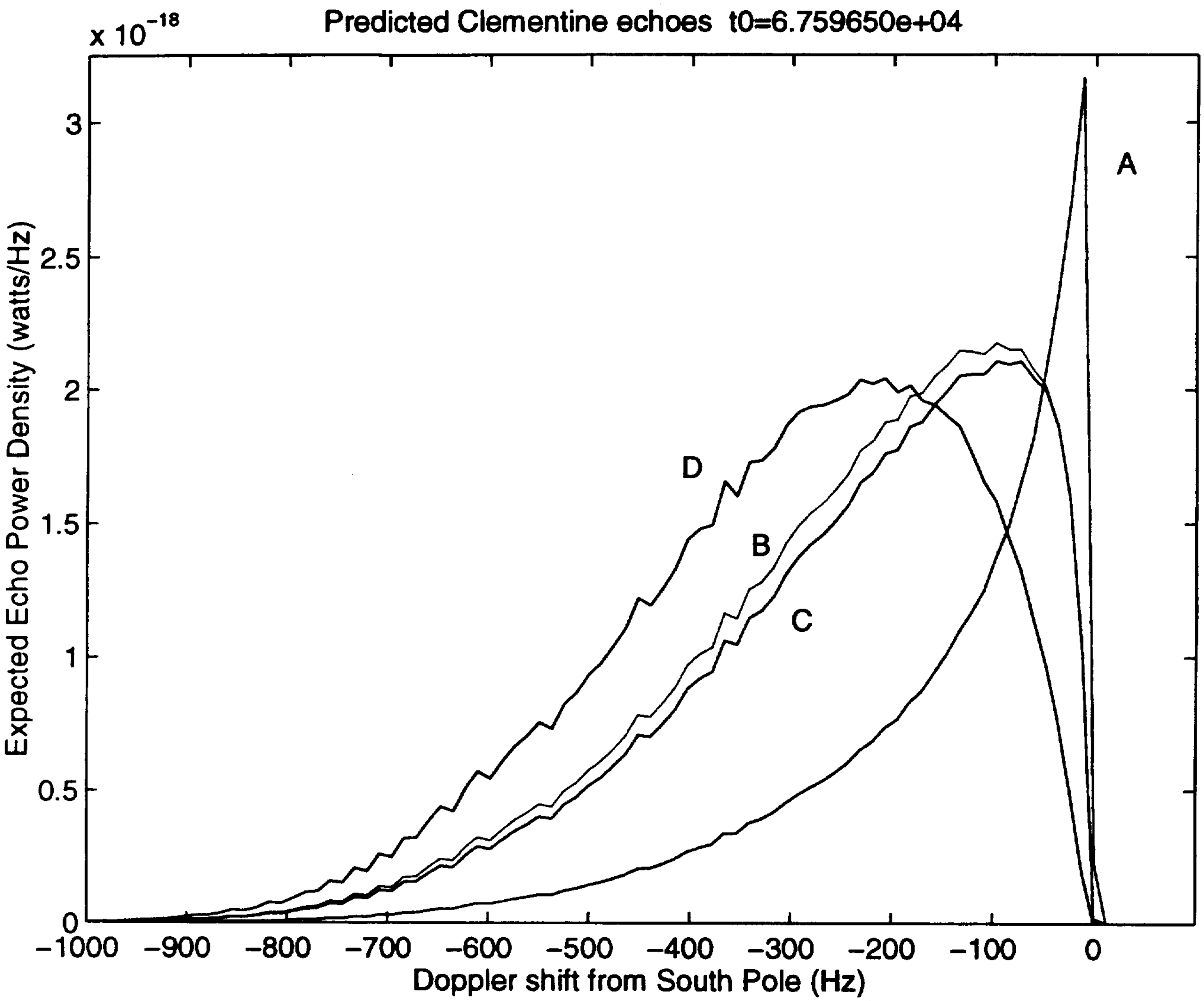
Predicted Clementine echoes t0=6.759650e+04
x 10^{-18}
Expected Echo Power Density (watts/Hz)
3
2.5
2
1.5
1
0.5
0
−1000
−900
−800
−700
−600
−500
−400
−300
−200
−100
0
Doppler shift from South Pole (Hz)
A
B
C
D

Figure 11

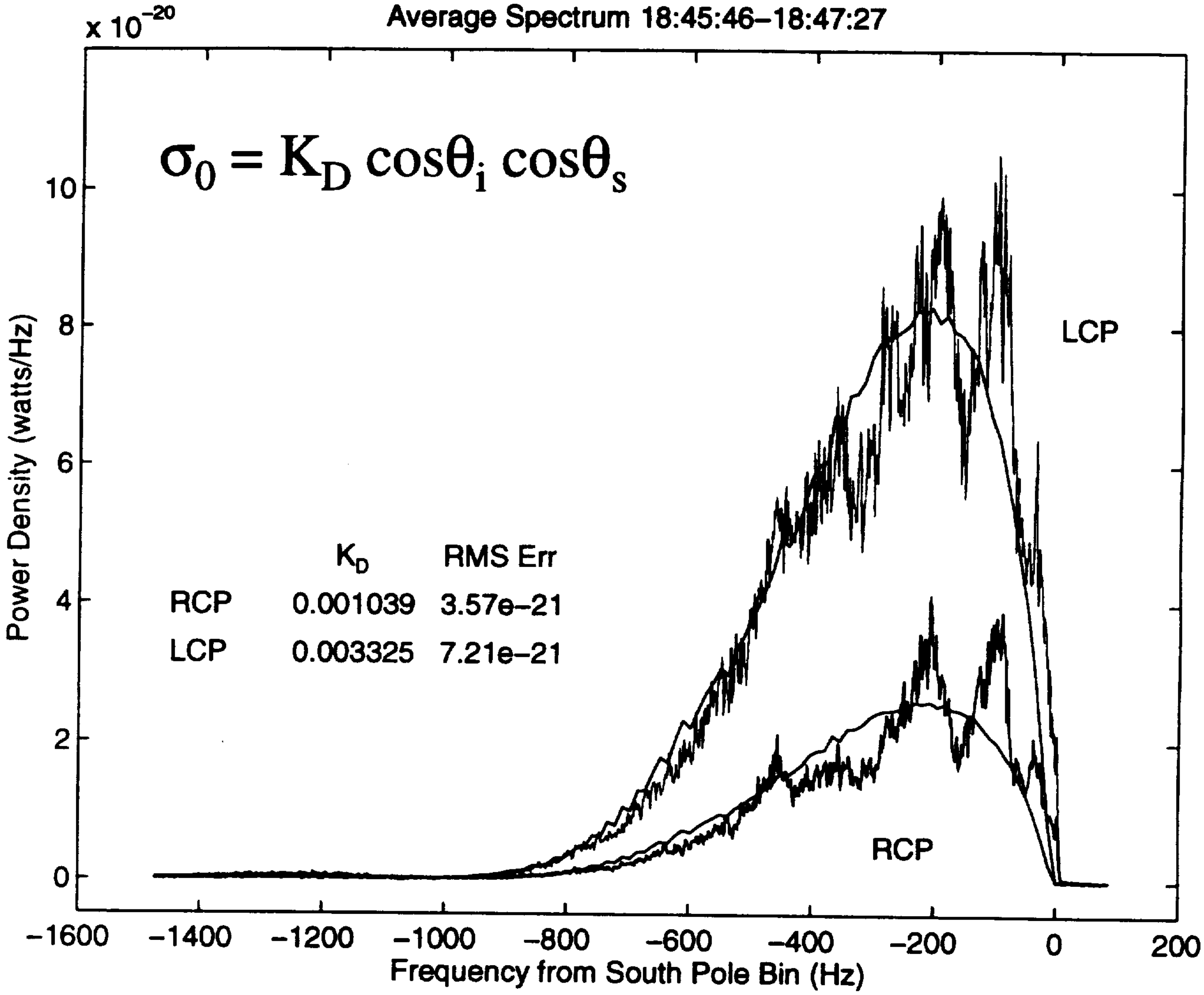
Average Spectrum 18:45:46–18:47:27
x 10^-20
$\sigma_0 = K_D \cos\theta_i \cos\theta_s$
K_D RMS Err
RCP 0.001039 3.57e–21
LCP 0.003325 7.21e–21
LCP
RCP
Power Density (watts/Hz)
0
2
4
6
8
10
−1600
−1400
−1200
−1000
−800
−600
−400
−200
0
200
Frequency from South Pole Bin (Hz)

FIGURE 12